DETECTION OF ICE AND DE-ICING/ANTI-ICING FLUIDS ON AIRCRAFT SURFACES USING TIME DOMAIN REFLECTOMETRY

A THESIS
SUBMITTED TO THE FACULTY OF
UNIVERSITY OF MINNESOTA
BY

EVAN ANDERSON

IN PARTIAL FULFILLMENT OF THE REQUIREMENTS
FOR THE DEGREE OF
MASTER OF SCIENCE

DR. JOHN EVANS

MAY 2014

Acknowledgements

The progress I have made on this project would not have been possible without the support and guidance Dr. John Evans has provided over the past five years. His support has been instrumental in my decision to pursue a career in academic research. Additionally, I would like to thank Luke Busta for sharing his knowledge of the project during my undergraduate career.

Dedication

This thesis is dedicated to my supportive and loving fiancé and family.

Abstract

Time domain reflectometry is a practical and effective way to detect ice, frost, moisture, anti-icing/de-icing aircraft fluids (ADAFs), and mixtures of each on aircraft surfaces. Using this method, a passive sensor is placed at the end of a transmission line. A fast rise-time pulse excites the transmission line and is reflected from the sensor upon its arrival at the end of the line. The detailed shape of the reflected waveform depends on the dielectric properties of the fluid in contact with the sensing electrodes. Multiple sensors were constructed and tested to determine the suitability and reliability of varying designs. A software protocol was also developed to detect phase transitions and alert pilots with a binary response that indicates a safe or hazardous condition. In effect, this system would help reduce the volume of ADAFs applied and increase the safety of air travel.

Table of Contents

List of Tables

List of Figures

Chapter 1. Introduction

1.1 Motivation for Study

Frost and ice accumulation on aircraft surfaces reduces lift and alters in-flight characteristics leading to an increased risk of accidents.[1,2] In inclement weather, formulated anti-icing/de-icing aircraft fluids (ADAFs) are used to remove and prevent the build-up of ice and snow on aircraft surfaces. Aircraft de-icing is achieved with Type I fluids consisting of 80% glycols, 20% water, and corrosion inhibitors – colored orange. Type I fluids are typically heated and sprayed under pressure onto aircraft surfaces to remove accumulated ice and snow. Once ice and snow have been removed, Type IV fluids consisting of 50% glycols, 50% water, pseudoplastic thickeners, and corrosion inhibitors – colored green are sprayed under pressure onto aircraft surfaces to prevent frost and ice formation during extended periods of time. They are used for anti-icing because they provide a protective layer for precipitation to buildup on, and they allow accumulated precipitation to slide off during takeoff. Due to the necessity of aircraft de-icing and anti-icing, large volumes of ADAFs are applied at numerous national and international airports. At the Lester B. Pearson International Airport in Toronto, ON three million liters of ADAFs were applied during the 1995-1996 season.[3]

After an aircraft has been de-iced and anti-iced, pilots rely on a large number of Federal Aviation Association (FAA) holdover time tables to determine a time window during which an aircraft is safe for takeoff. They are based on air temperature, precipitation type, precipitation intensity, wing surface, de-icing procedure, fluid manufacturer, fluid dilution, and fluid type. Due to a large variability in holdover times for a given condition, the pilot is ultimately responsible for determining when to takeoff. Often, pilots rely on

visual inspection of the aircraft to determine if frost and ice have accumulated. They rely on the color of both Type I and IV fluids to aid in visual inspection (Figure 1.1).

Figure 1.1 Picture of a sufficient coating of Type IV fluid on an aircraft wing.

Currently, there have been a variety of instrumental approaches used for the detection of ice on aircraft surfaces. These approaches have employed sensors based on radioactive, conductimetric, differential-pressure, magnetostrictive, piezoelectric, and fiber-optic techniques.[4] While these systems are able to reliably detect ice, and in some cases ice thickness, they use expensive sensing techniques. Additionally, they have not been widely implemented by aircraft manufacturers, and pilots still rely on holdover time tables and visual inspection as the main indicator of frost and ice accumulation.

The goal of this investigation was to demonstrate that time domain reflectometry (TDR) is an effective, reliable, and cost-effective technique for determining the condition of aircraft surfaces. In addition to detecting ADAFs, ice, frost, water, air, and mixtures of

each, the sensing system should be able to detect phase transitions, which could be used to alert pilots and ground personnel with a binary output indicating a safe or hazardous condition. It was hoped that this system would not only help reduce the volume of ADAFs applied each season, but would increase the safety of aircraft travel by adding conclusive information pilots can rely on during inclement weather.

1.2 Time Domain Reflectometry Background

TDR involves applying a fast rise-time (ps time frame) voltage pulse to one end of a transmission line.

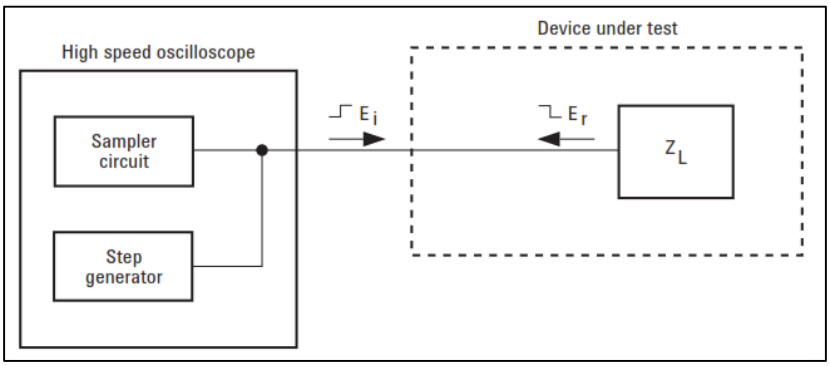

Figure 1.2 Schematic of a time domain reflectometer.

The pulse travels down the transmission line at a velocity nearing the speed of light, which depends on the dielectric properties (or permittivity) of the medium surrounding the transmission line, according to:

$$\upsilon = c / \sqrt{\varepsilon} = c / n \qquad (1)$$

where, c is the velocity of light in vacuum, ε is the dielectric constant of the medium surrounding the transmission line, and n is the complex refractive index of that medium. Any point along or at the terminus of a transmission line where the impedance changes (due to a change in dielectric constant of the surrounding medium) a portion of the energy in the pulse is reflected back to the source. That portion of energy not absorbed or reflected at a discontinuity continues down the line until it is either absorbed or reflected. The reflected pulses are then acquired using a sampling circuit at a sub-nanosecond timescale. Using equation 1, reflections/impedance changes measured by TDR can be traced back to their physical location along the transmission line.

For example, consider a segmented system as shown in the following figure:

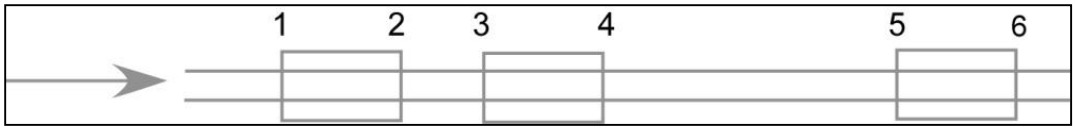

Figure 1.3 Transmission line with six dielectric discontinuities. The gray boxes around segments 1-2, 3-4, and 5-6 indicate a dielectric different from that in segments 2-3 and 4-5.

As the launched pulse encounters each dielectric discontinuity, a portion of the energy is reflected back to the source. In addition to determining the locations of the impedance mismatches by measuring the time it takes for a reflected pulse to be acquired, the shape of the pulse also contains information about the type and magnitude of the source of the impedance change. This information content has allowed TDR to be the primary technique used to test electrical interconnects and transmission lines in high speed circuitry (e.g. serial disk drive communication protocols, Ethernet cabling systems, etc.).

For simple impedance mismatches (where only real impedance is considered here), the nature of the reflected pulse can be analyzed according to:

$$\rho = \frac{E_r}{E_i} = \frac{Z_L - Z_0}{Z_L + Z_0} \tag{2}$$

where, ρ is the reflection coefficient, E_r is the magnitude of the reflected pulse, E_i is the magnitude of the incident pulse, Z_L is the impedance of the load, and Z_0 is the impedance of the transmission line. If there is no difference between Z_0 and Z_L, the pulse will not be reflected and only the incident pulse will be measured.

If the impedance of the load, Z_L, is significantly higher that the impedance of the of the transmission line, Z_0, the majority of the pulse will be reflected (Figure 1.4).

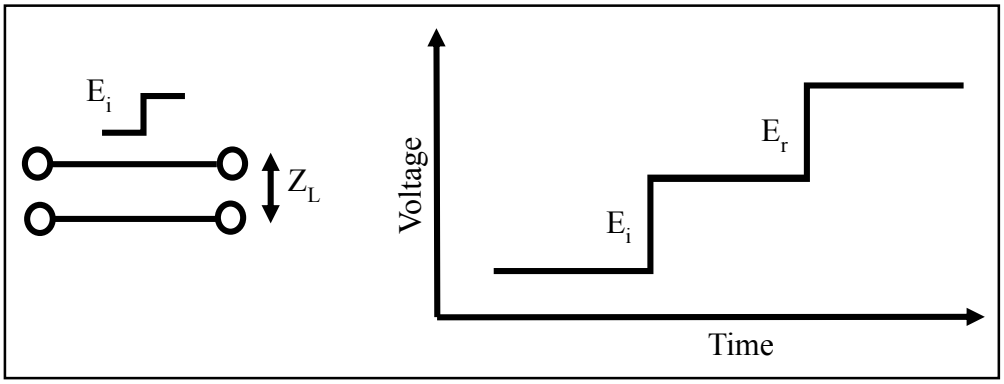

Figure 1.4 Open circuit termination measured by TDR.

In a closed circuit, the transmission line will have a greater impedance than the load, or $Z_L=0$. In this case, the reflected pulse will be algebraically subtracted from the incident pulse (Figure 1.5).

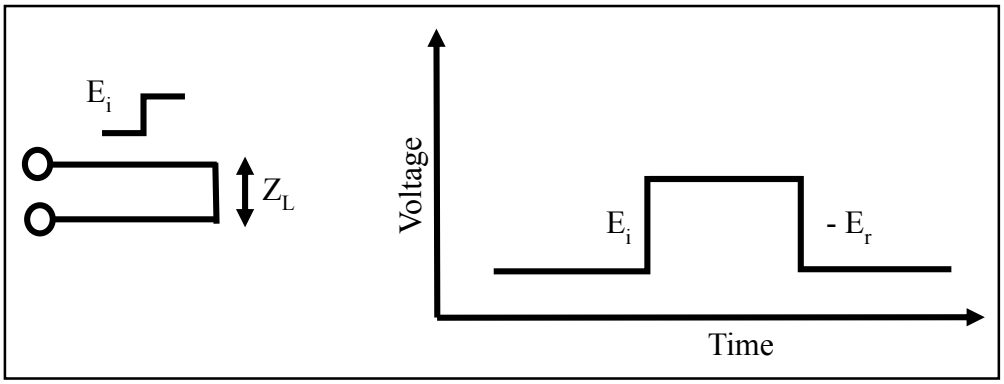

Figure 1.5 Closed circuit termination measured by TDR.

1.3 Chemical Sensing Using Time Domain Reflectometry

Due to the sensitivity of TDR to changes in the impedance of a transmission line (including dielectric properties), simple sensing systems can be realized as shown in Figure 1.6.

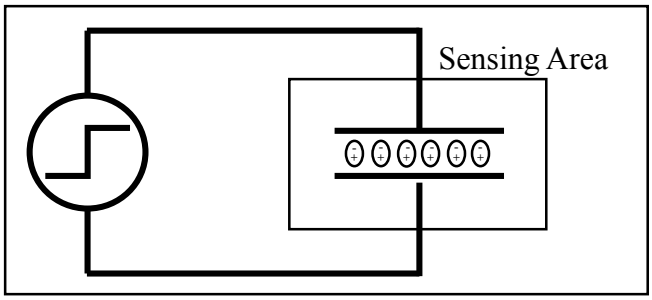

Figure 1.6 Diagram of a simple sensing system, a parallel plate capacitor.

Examples of recent applications of this technology to sensing include measurement of resin flow in polymer curing applications,[5] water and ice content in soil systems,[6,7,8] and detection of ice, water, and deicing solutions on aircraft wings and rotors over wide areas.[8] Due to the ease with which dielectric relaxation measurements can be made over such a wide frequency range, 1 MHz to 20 GHz, TDR has been applied to fundamental research involving the structure of water[10] and the relaxation of water bound to silica gel.[11]

For the simple capacitor, due to the fast rise-time pulse used in TDR, a broad range of frequencies is present that excites a medium between the plates. When an electric field is applied to a dielectric medium, induced and permanent dipoles orient between the electrodes of the transmission line. In addition to the orientation of dipoles, charged particles are attracted or repelled from the sensing electrodes. Each of these processes attenuates some of the frequency content contained within the excitation pulse. These processes have been widely studied in the field of dielectric relaxation spectroscopy (DRS). DRS experiments employing TDR differ from those using standard DRS techniques due

to the excitation process. TDR techniques use a fast rise time pulse to excite the medium, while standard DRS techniques scan the frequency range of interest.

The frequency content of a reflected pulse contains information that is characteristic of the complex dielectric function of the medium in contact with the sensing electrodes (Figure 1.7).

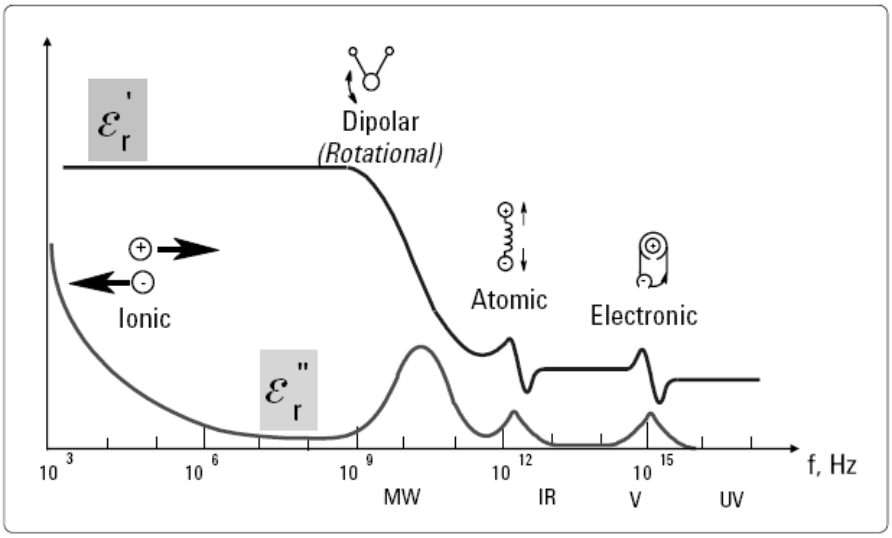

Figure 1.7 Illustration of the complex dielectric function. The real part (ε_r') of the complex dielectric function represents the energy lost and imaginary (ε_r'') component represents the energy stored.

Using the information contained within a reflected pulse, a determination of the dielectric medium can be made by attributing the information to materials for which the dielectric properties have been previously calibrated (e.g. water, ice, frost, and ADAFs) using methods as straightforward as correlation (Figure 1.8).

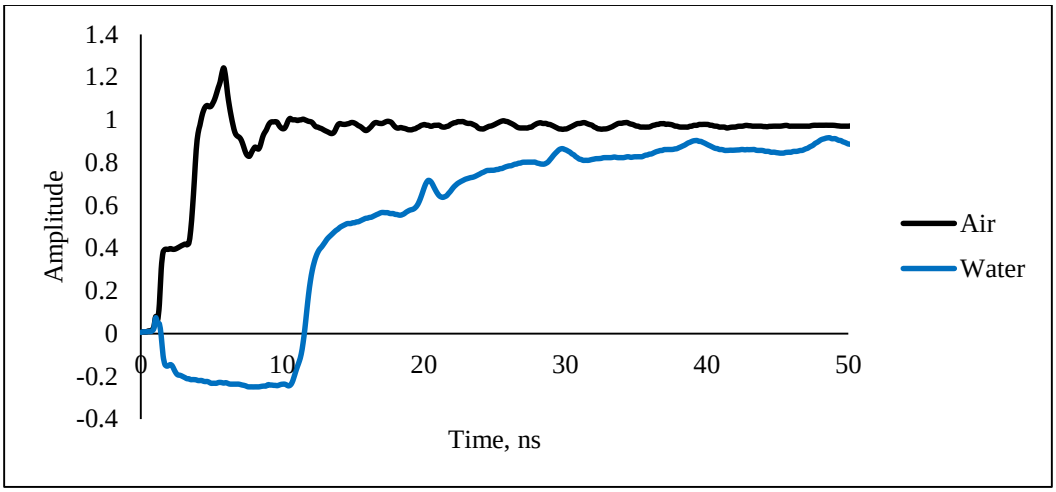

Figure 1.8 Reflected pulses collected from a parallel electrode sensor immersed in air and water. The two pulse can be reliably distinguished by correlation with standard reflections.

Chapter 2. Experimental

2.1 Test Chamber

In order to test TDR as a sensing technique and varying sensor designs under simulated environmental conditions, a test chamber was designed to control the temperature of the sensor and overlaying solutions to ± 1°C.

Temperature controlled experiments were conducted in an insulated container with both a model AC-194 Peltier air cooler/heater and model CP-200TT cold plate made by TE Technology Inc. The air cooler/heater was mounted in the lid of the container and the cold plate up through the bottom of the container. Power and temperature control was provided and accomplished by power sources and temperature controllers also from TE Technology Inc. A block diagram of the test system is shown in Figure 2.1.

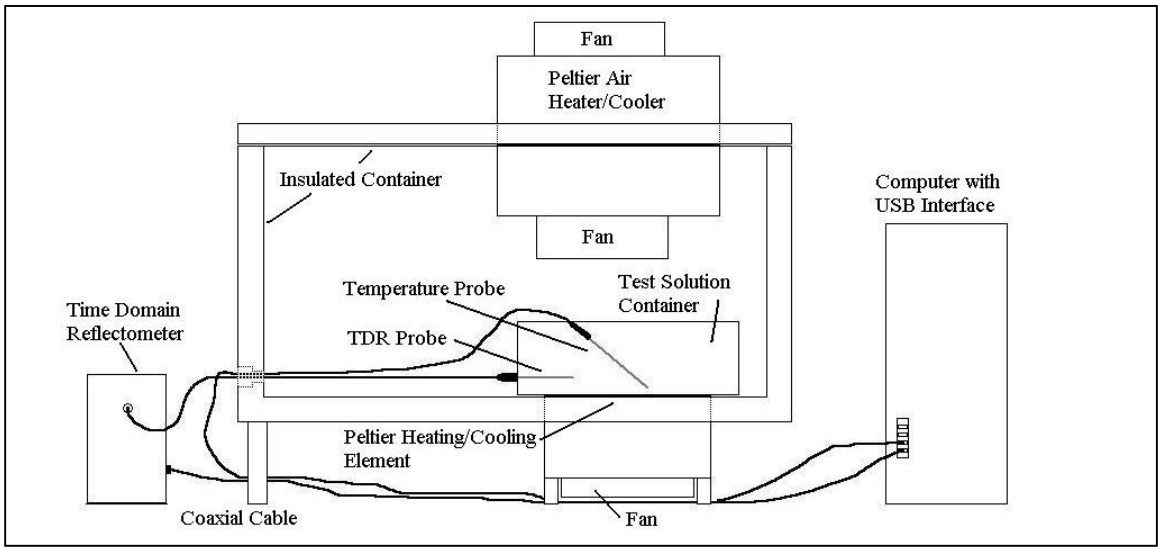

Figure 2.1 Block diagram of a temperature controlled test stand.

The sensor being tested was placed on the Peltier heating/cooling element. A temperature probe purchased from Vernier was also placed on the sensor to provide temperature readings of the sensor and chamber as it was cooled or heated. Temperatures

well below freezing were obtainable when given proper time, and dry ice was often placed in the container to speed the process.

2.2 Data Acquisition and Hardware

Data acquisition was carried out using a Campbell Scientific TDR100 time domain reflectometer, CR1000 datalogger, and SDMX50SP multiplexer. The multiplexer allowed for multiple sensors to be tested under uniform conditions. The CR1000 datalogger was connected to a PC via an Ethernet connection. The software program LoggerNet, from Campbell Scientific, provided programming, communication, and data retrieval between the datalogger and PC. The entire system is presented below.

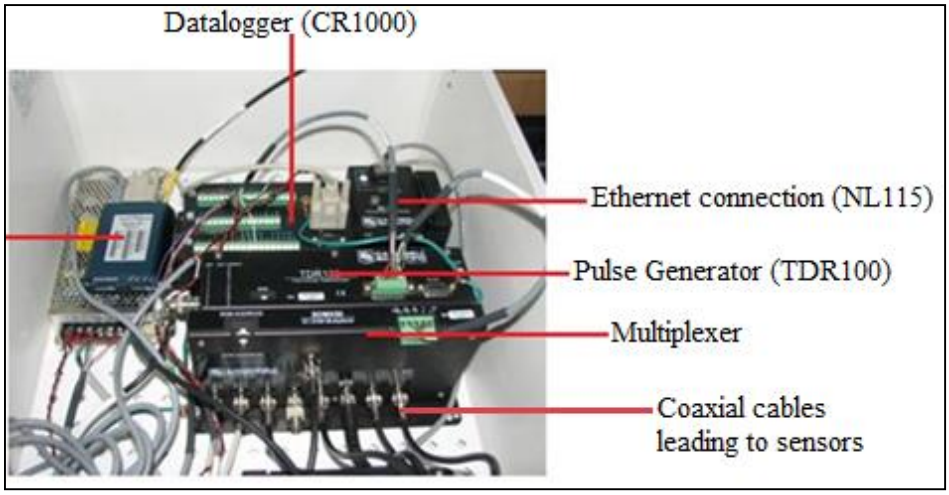

Figure 2.2 Campbell Scientific TDR equipment.

Data was collected from candidate sensors every minute, including temperature. Sensors were covered with a specific medium, and the test chamber was heated or cooled until the desired temperature was reached. The collected files were then compiled and saved for later manipulation. These files contained the time, temperature, and LoggerNet parameters.

In order to manipulate the data acquired and develop a software protocol, National Instrument's LabVIEW was used. With this program, simple and advanced signal processing techniques were able to be implemented during data processing.

2.3 Sensor Design

The general approach to sensor design was intuitive rather than being based on detailed electrodynamic modeling of the conducting elements and dielectric gap of the sensor. General aspects considered were drawn from previous experiments on bridge surface sensors[12] and included the following:

1. Electrode Gap
2. Electrode Surface Area
3. Electrode Length

In contrast to the previous study, more intricate sensors could be designed and tested due to the reduced ruggedness of an aircraft surface as compared to a bridge or road surface.[12] This lead to the use of circuit board traces as sensing elements (Figure 2.3).

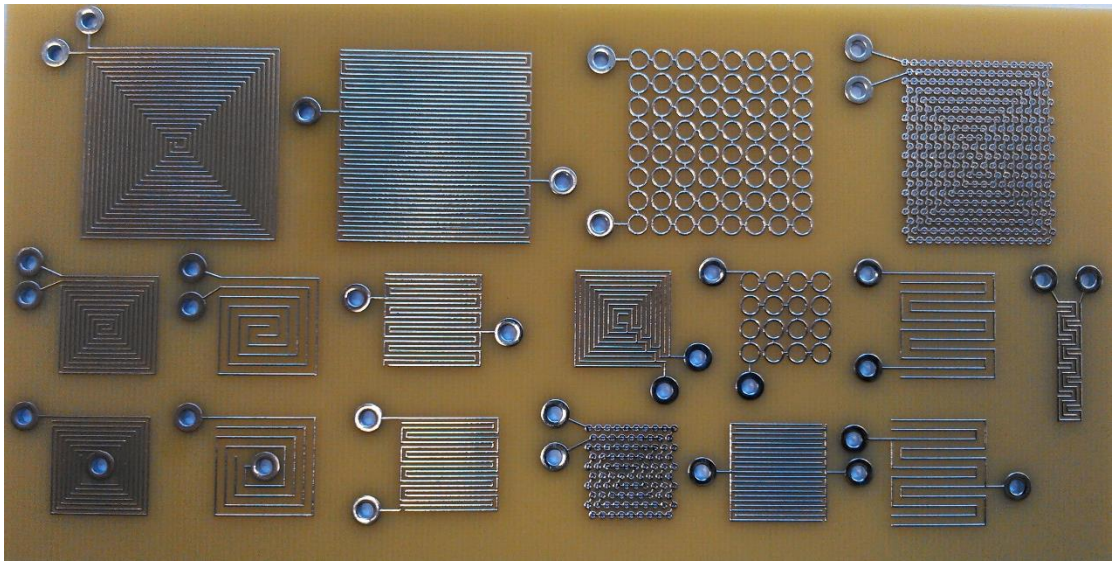

Figure 2.3 Printed circuit board sensor designs. The large sensors are 1" by 1" and the small sensors are 0.5" by 0.5". Sensors were connected to the TDR by soldering to 50Ω coaxial cable.

In each case fitting of 50 Ω BNC female connector to connect to the cable from the TDR source was required. Four sensors were tested simultaneously to insure that conditions and temperatures were uniform during testing.

2.4 Optimization of Time Domain Reflectometry Acquisition Parameters

When acquiring raw data (reflected TDR transients) from a candidate sensor, four parameters were important to optimize: averages, points, start, and length. Average input can vary from 1 to 128 averages, and it is the number of separate waveforms that the TDR100 averages together to calculate the displayed waveform. Standard files were taken at 8, 16, 32, and 64 averages while keeping the other three parameters constant to test which value would lead to the greatest correlation between a sample file and a previously acquired standard. Diminishing returns were found after 16 averages. The number of points employed to represent the transient responses can vary from 2 to 2048 points and this parameter determines the data density of the acquired waveform. Standard files were taken with 256, 512, 1024, and 2048 points while keeping the other parameters constant. It was found that 512 points was optimum when correlating sensor calibration files with unknown sample files in real time. From these tests 16 averages and 512 points became the routine parameters for calibration and testing candidate sensors.

The delay times before the start of an acquisition cycle was optimized by gathering the waveform shortly before the first reflection from the sensor so that a baseline reference level could be included in the file. The length for the acquisition of each waveform was optimized by using a value that would allow the waveform voltage to approach a steady state value at the end of the data vector representing the transient response as shown in the following figure:

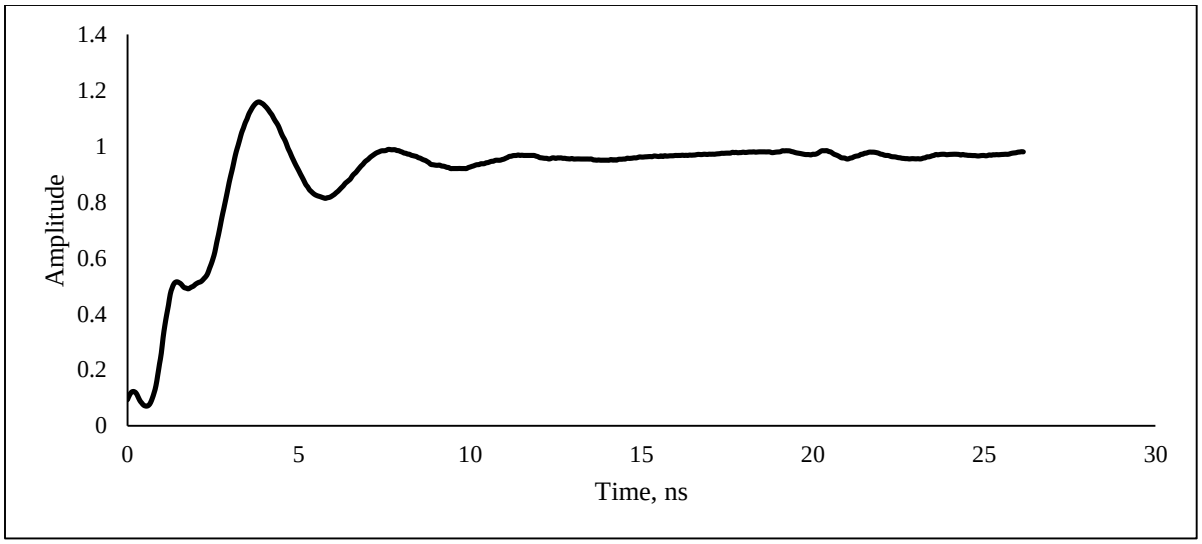

Figure 2.4 Raw data from a candidate sensor showing a steady state value at the end of the data vector.

Chapter 3. Sensor Evaluation During Steady State Conditions

3.1 Development of a Quantitative Indicator of Sensor Performance

In order to demonstrate time domain reflectometry as a reliable technique for the determination of media in contact with a passive sensor, a quantitative indicator of sensor performance was developed. Initially, steady state conditions were used to simplify the determination of sensor surface conditions.

Sensor performance was determined by coving a candidate sensor in and acquiring standard responses (waveforms) of air, water, ice, 50/50 Type I/water (by volume), and 50/50 Type IV/water (by volume). The raw TDR transient waveforms were differentiated, followed by digital filtering employing a Savitzky–Golay filter (21 point, 3rd order polynomial) to reduce noise introduced by differentiation.

The sensor waveform under test was then correlated against known standard responses (previously determined under known conditions; i.e. exposure to air, ice, water, etc.) for that sensor. The correlation coefficient returned from this correlation (R^2_{der}) yielded values ranging between 0 (uncorrelated) to 1 (perfectly correlated). The most challenging differentiation for all candidate sensor designs was found to be between ice and air for the media in contact with the sensor electrodes.[12]

To improve upon the ability of a sensor to identify the medium in contact with its electrodes, a more sophisticated data analysis approach was taken. This included the analysis of frequency content of the differentiated and smoothed TDR waveforms for both standard and unknown media responses. Typically Fourier analysis is used for this purpose.[13] An improved approach, the wavelet transform, which uses more complex base functions called wavelets as opposed to the sine-cosine functions employed in the case of

the Fourier transform was implemented.[14] Uses of wavelets in signal processing include noise reduction, data compression, peak detection, and time-frequency analysis. Advantages of wavelet transformation over the Fourier transform include multiresolution properties introduced by the dilating process and the characteristics of the mother wavelet make this technique suitable for representing functions with sharp peaks and non-periodic signals, which is precisely what was seen in the waveforms returned from the candidate sensors. Low-frequency signals require fine frequency resolution whereas high-frequency signals require fine time resolution; hence, analysis of signals with high and low frequency content must be performed with a technique with multiresolution properties to be effective.

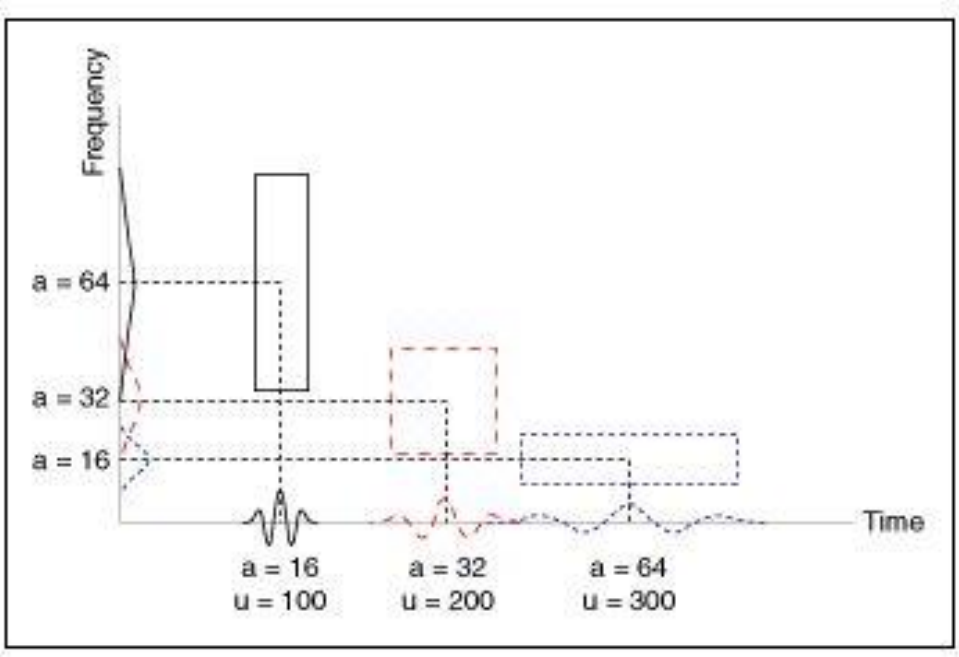

Figure 3.1 A depiction of the wavelet transform's ability to provide variant resolution where necessary in both the frequency and time domains. The widths of the boxes represent the time and frequency resolutions of the same wavelet with various scaling. A wavelet with small scale (a=16) displays fine time resolution and coarse frequency resolution. Conversely, a wavelet with large scale (a=64) has the opposite properties. The variable 'u' corresponds to the location of the center of the wavelet on the x-axis.

The use of a "mother" wavelet which is scaled in time has been shown to provide more robust frequency analysis without the frequency resolution issues that accompany Fourier analysis.[15]

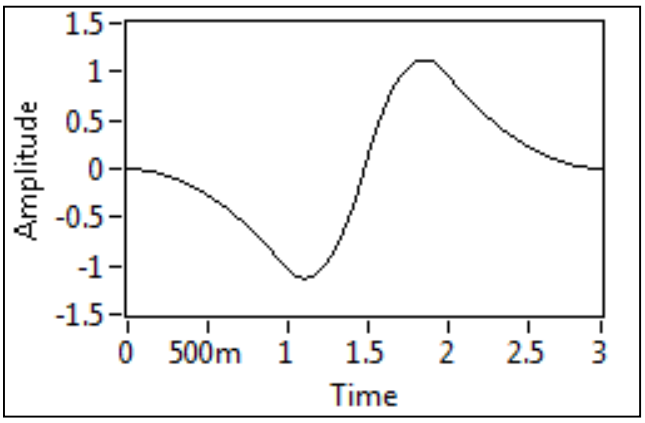

Figure 3.2 The Biorthogonal 3.1 wavelet. This wavelet was selected from a large bank of wavelets as it produces the best decomposition of the signals received from the candidate sensors.

While the wavelet transform has been most widely applied to image processing[16,17] and comparisons between this approach and Fourier-based methods have been drawn,[18] its current use for this project is relatively simple. To obtain a relatively global indication of high and low frequency content of the smoothed derivative TDR waveforms reported by a sensor, a wavelet transformation obtains a snapshot of the low and high frequency content of these via a multiscale analysis (trending analysis). As such each smoothed derivative TDR waveform (sample as well as standards) is subjected to such analysis as implemented in LabVIEW. The low and high frequency content for a sample waveform is then correlated with its standard counterpart to give two additional regression coefficients R^2_{hf} and R^2_{lf} for the high and low frequency components, respectively. Each of these ranges between 0 (uncorrelated) to 1 (perfectly correlated), similarly to R^2_{der}, discussed above. Finally these three correlation coefficients are added together to obtain the figure of merit (FOM) for a given comparison of sample to standard for a calibrated sensor. This FOM ranges from 0

to 3 and is taken as the single indicator of best match between sample (unknown surface condition) and standard (previously calibrated response to a known surface condition). Figure 3.3 depicts the approach.

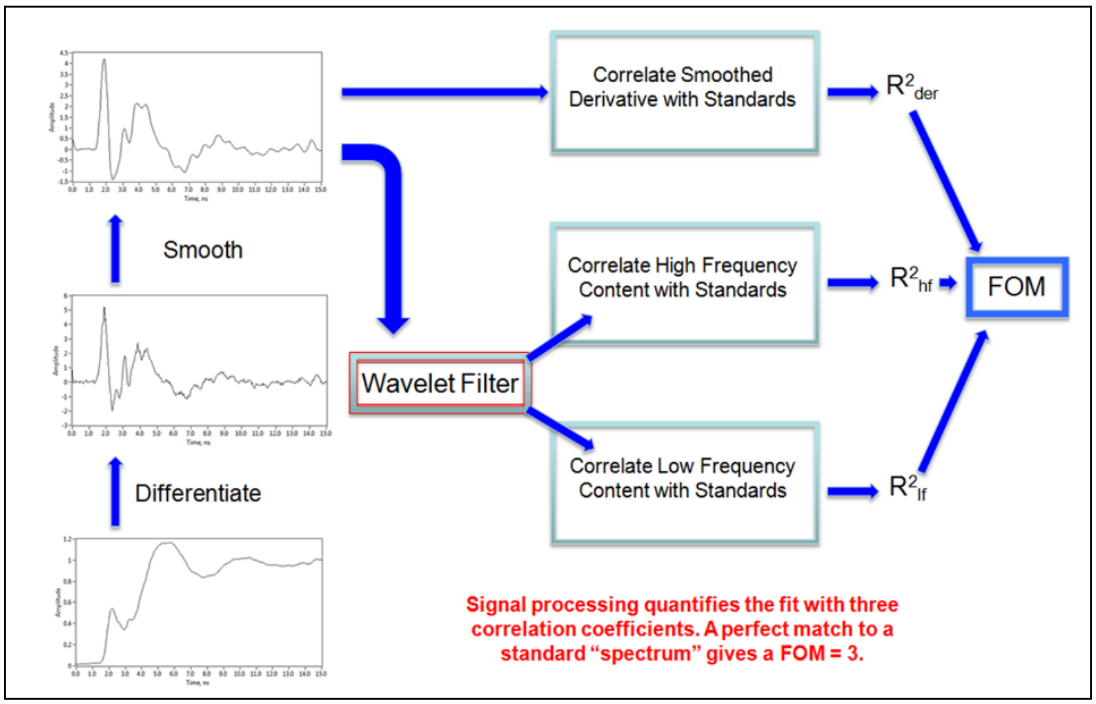

Figure 3.3 Overall signal processing scheme yielding a single real-time figure of merit (FOM) for sensor response correlated against bank of standards.

To demonstrate the necessity of the FOM, two sensor cases are presented below.

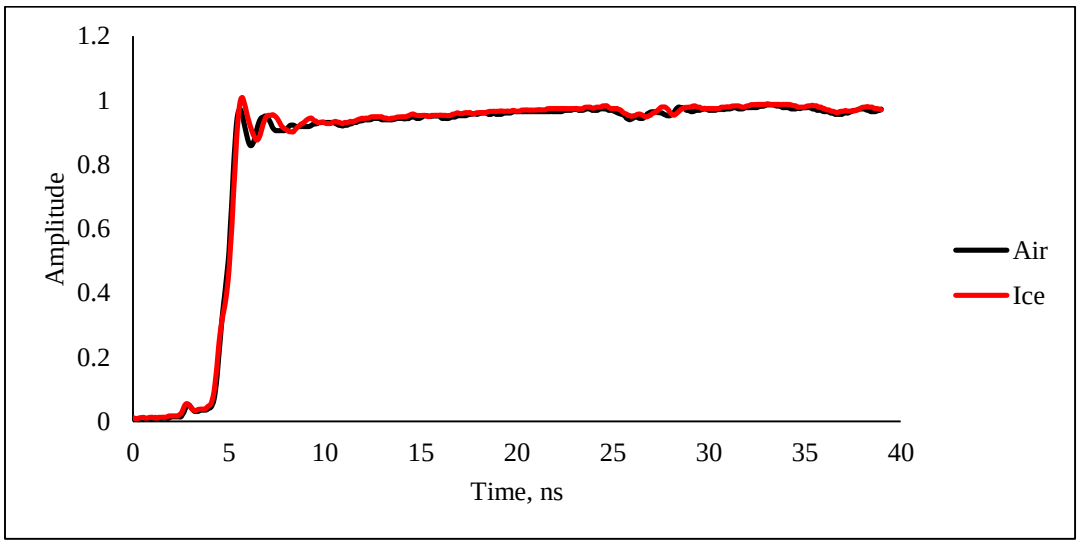

Figure 3.4 Example of poor data from a candidate sensor.

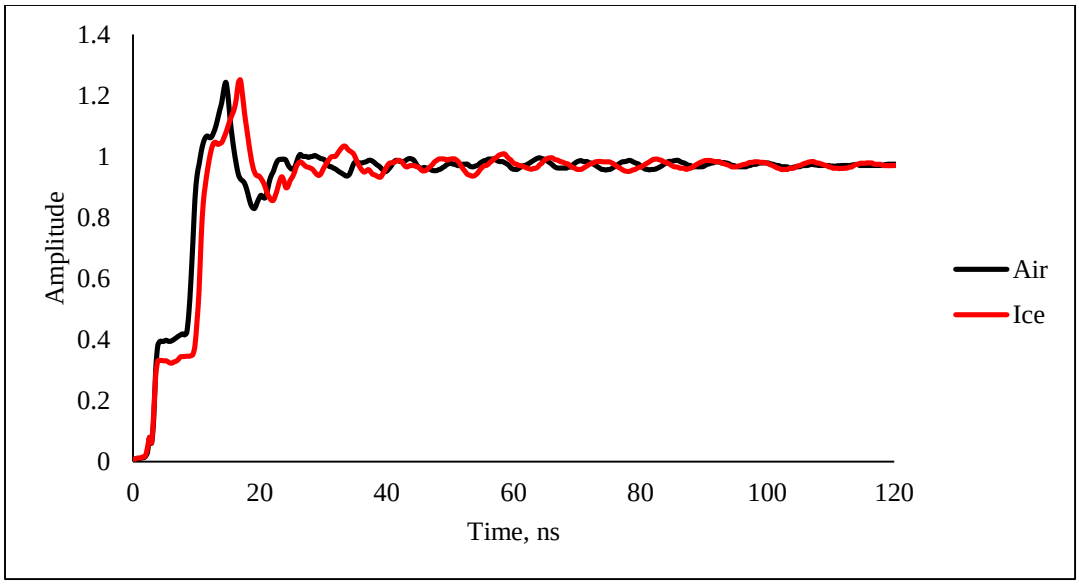

Figure 3.5 Example of good data from a candidate sensor.

To compare sensors of varying shapes and sizes, correlation arrays were calculated for each sensor. These correlation arrays include the figure of merit, out of three, of each standard correlated against all other standards. These correlation arrays allow for an easy determination of sensor performance.

Table 3.1 Example of a bad sensor correlation array.

	Air	Water	Ice	Type I (50-50)	Type IV (50-50)
Air	3.000	1.109	2.917	0.747	1.066
Water	1.109	3.000	1.091	2.621	2.828
Ice	2.917	1.091	3.000	0.720	1.067
Type I (50-50)	0.747	2.621	0.720	3.000	2.871
Type IV (50-50)	1.066	2.828	1.067	2.871	3.000

Table 3.2 Example of a good sensor correlation array.

	Air	Water	Ice	Type I (50-50)	Type IV (50-50)
Air	3.000	0.072	1.210	0.030	0.142
Water	0.072	3.000	0.084	0.610	1.850
Ice	1.210	0.084	3.000	0.087	0.143
Type I (50-50)	0.030	0.610	0.087	3.000	1.875
Type IV (50-50)	0.142	1.850	0.143	1.875	3.000

3.2 Additional Sensor Evaluation Using Figure of Merit

Correlation arrays were generated for each sensor, and sensors with the best performance were tested under additional conditions that would be present on an aircraft surface. These tests were conducted in order to characterize the response of varying sensor geometries and designs (Appendix A and B) and in order to select a candidate sensor for the continued testing presented in chapter 4.

3.2.1 Sensor Coating

Candidate sensors were coated with thin layers of a clear gloss spray paint in order to prevent corrosion of the electrode surfaces. The thin coatings effectively inhibited conductance between the electrodes and reduced the electric field penetration into the sample medium reducing the information content within the reflected pulse.

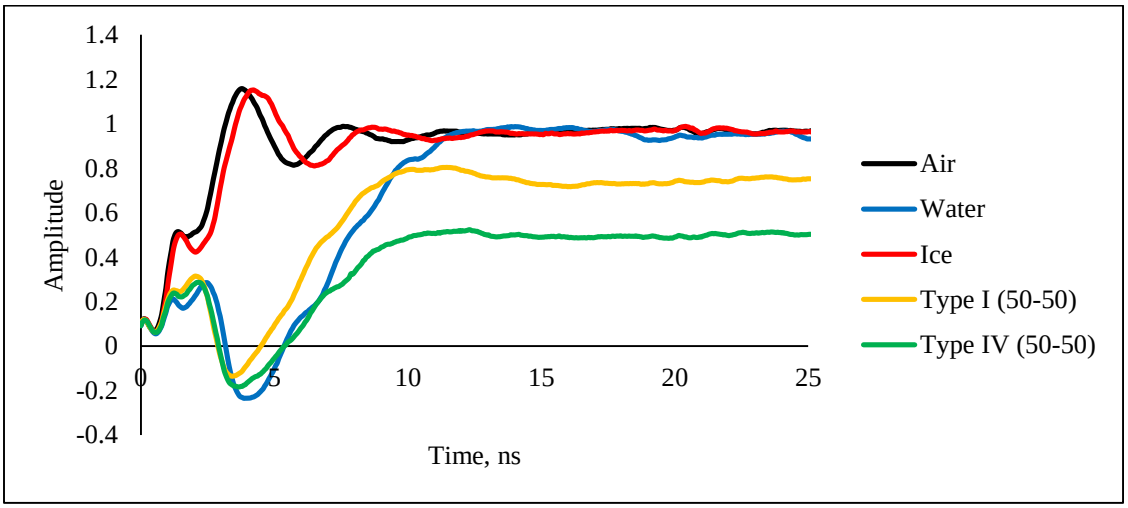

Figure 3.6 Standard waveforms collected by a candidate sensor with uncoated electrodes.

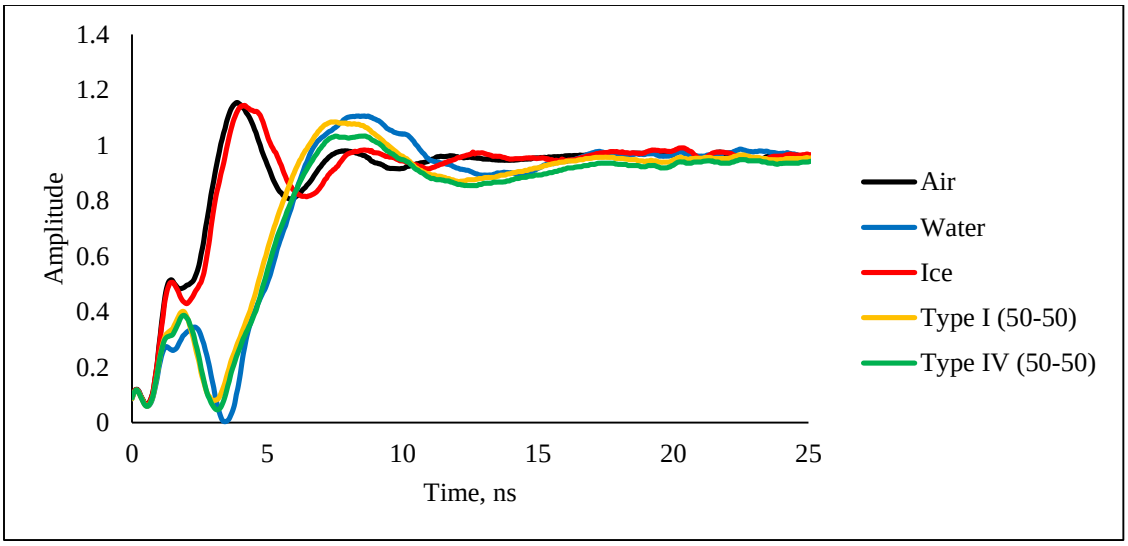

Figure 3.7 Standard waveforms collected by a candidate sensor with coated electrodes.

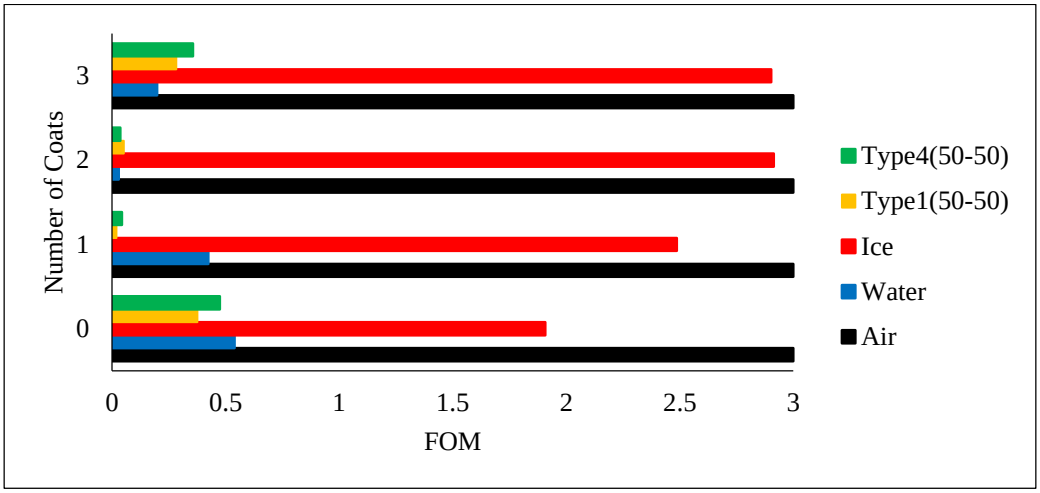

Figure 3.8 FOM variation as consecutive coats of a clear gloss spray paint were applied to a candidate sensor. All standards were correlated against an air standard to produce the displayed FOMs.

Figures 3.6 and 3.7 illustrate the reduction in conductance indicated by the steady state value of Type I and Type IV fluids at the end of data acquisition. Although these factors increased the FOM of air versus ice, acceptable FOM values were still obtained and ice and air were reliably distinguished (Figure 3.8).

A sensor with better performance than that shown in Figure 3.8 also did not exhibit a significant reduction in the differentiation between ice and air standards upon coating (Figure 3.9).

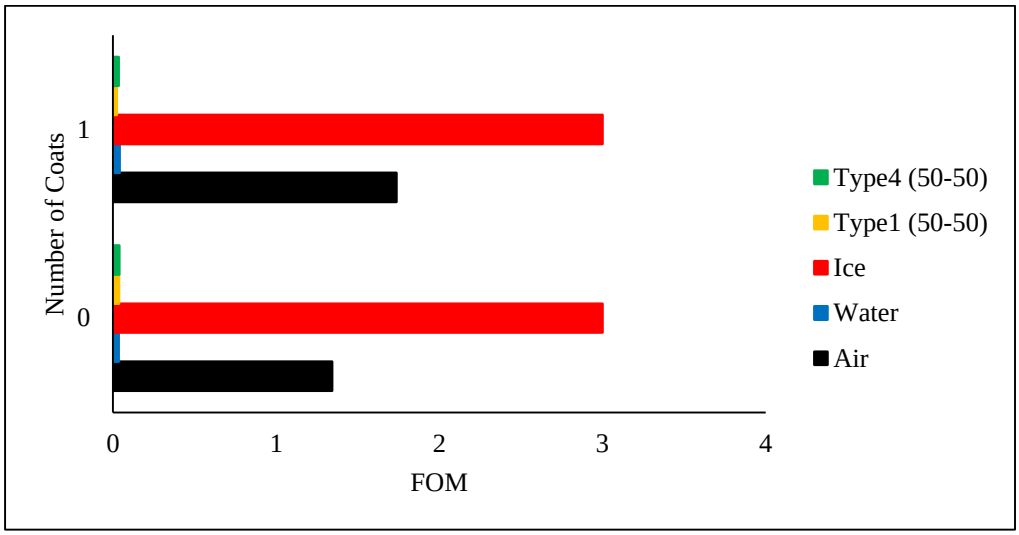

Figure 3.9 FOM variation as consecutive coats of a clear gloss spray paint is applied to a candidate sensor. All standards were correlated against an ice standard to produce the displayed FOMs.

3.2.2 Temperature of ADAFs

Changing the temperature of ADAFs applied to a candidate sensor leads to variation of the steady state value at the end of a transient waveform. This is due to the change in viscosity of the fluid with temperature. As the temperature of the fluid is increased, charge carriers are able to transfer charge at a faster rate. This effect is shown in the following two figures.

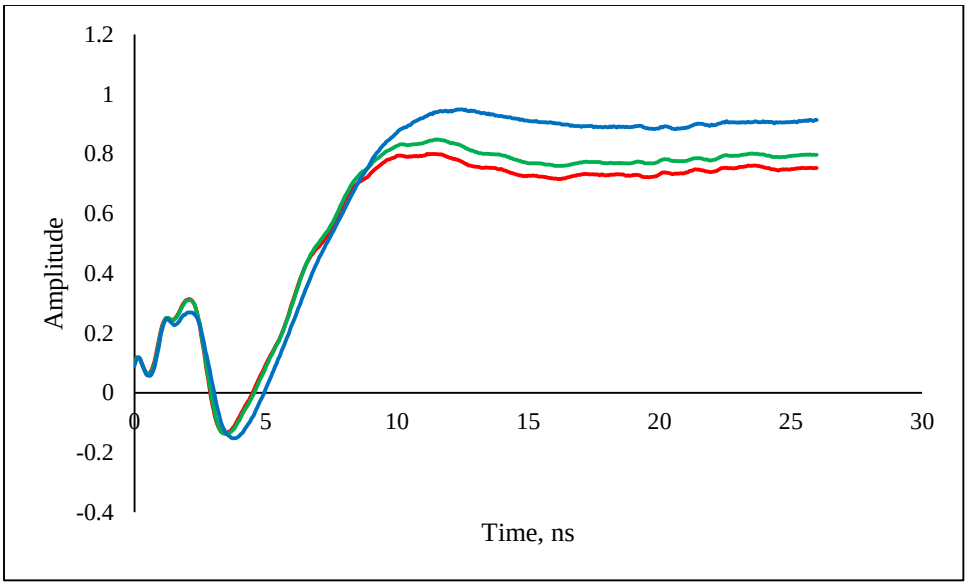

Figure 3.10 Waveforms collected with 50/50 Type I/water (by volume) in contact with a candidate sensor. Temperatures, from bottom to top, 60°C, 39°C, and 2°C.

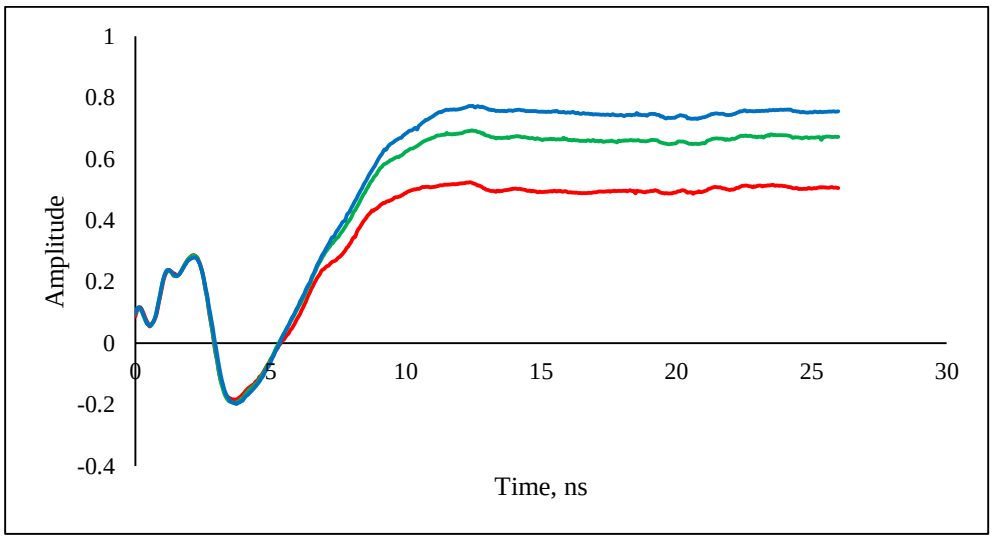

Figure 3.11 Waveforms collected with 50/50 Type IV/water (by volume) in contact with a candidate sensor. Temperatures, from bottom to top, 57°C, 22°C, and 7°C.

Although temperature effects the reflected waveforms with uncoated sensors, coated sensors do not exhibit this trend. Therefore, coated sensors were used to remove the temperature dependence and simplify experimental parameters. This is especially important as ADAFs are applied hot (100°C) and cool to ambient temperature.

3.2.3 Concentration of ADAFs

The concentration of ADAFs applied to an aircraft depends on the ambient air temperature, de-icing/anti-icing procedure, and fluid manufacturer. Therefore, the effect that the concentration of both Type I and Type IV fluids has on the resulting waveforms was studied. The waveforms acquired from 20/80 ADAF/water (by volume) and 100/0 ADAF/water (by volume) provide a FOM of 2.4 (Figure 3.12 and Table 3.3). This value is lower than that desired to indicate a positive determination of an unknown media. In order to account for this, multiple standard responses can be collected over a range of ADAF dilutions in order to accurately determine the media in contact with the passive sensor.

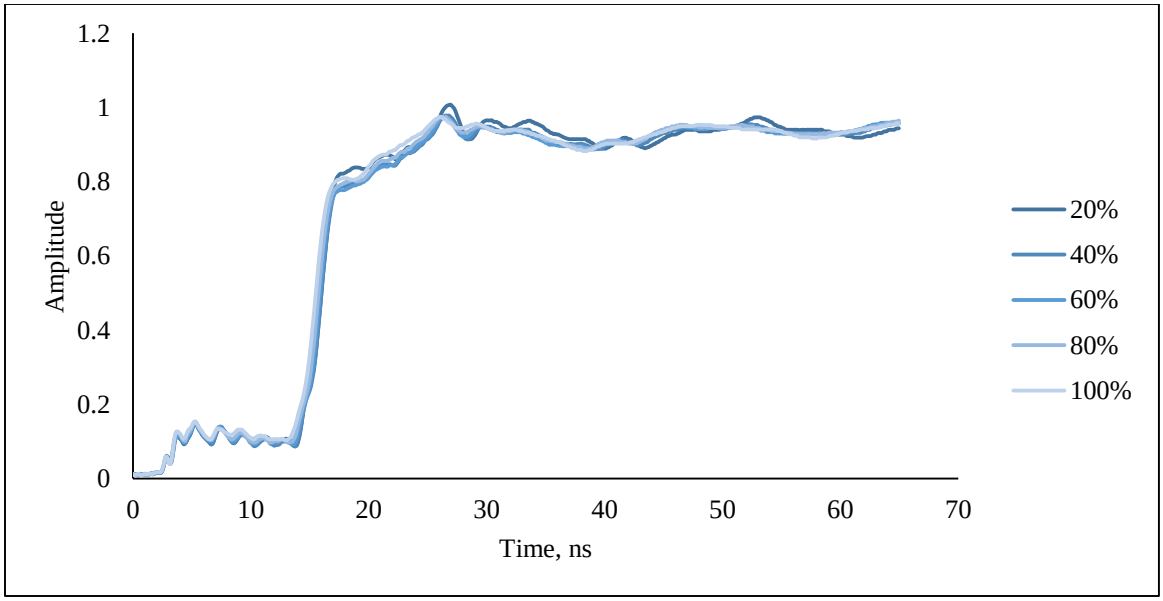

Figure 3.12 Waveforms collected with five dilutions of Type IV fluid.

Table 3.3 Correlation array with %Type IV fluid indicated.

	20%	40%	60%	80%	100%
20%	3	2.9553	2.8506	2.7447	2.3962
40%	2.9553	3	2.9595	2.8777	2.55999
60%	2.8506	2.9595	3	2.9663	2.7356
80%	2.7447	2.8777	2.9663	3	2.86941
100%	2.3962	2.56	2.7356	2.8694	3

3.2.4 Coating Thickness of ADAFs

The thickness of the medium in contact with the passive sensors does not greatly alter FOM values until the medium becomes discontinuous across the sensor electrodes. When sensors were covered with viscous Type IV fluids, sample waveforms were found to be consistent while the sensor was oriented vertically and the Type IV fluid flowed off (Figure 3.13). Sample waveforms were consistent because the sensor was continuously covered with uniform layer of Type IV fluid.

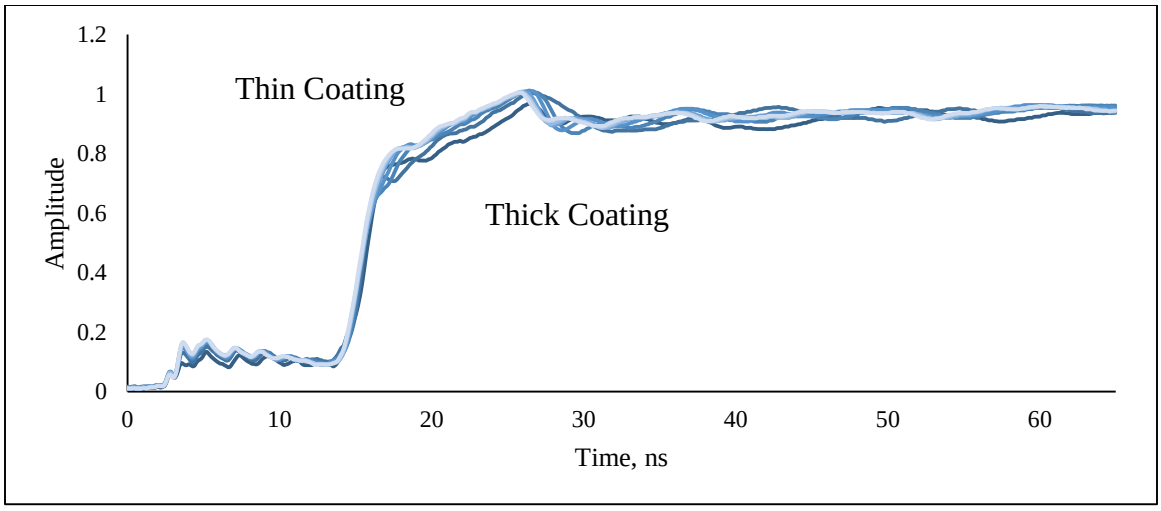

Figure 3.13 Waveforms collected from sensor B21 as Type IV fluid was applied and the sensor was oriented vertically to allow the fluid to flow off the sensor.

Waveforms were found to be inconsistent when sensors were coated with Type I fluid and oriented vertically allowing the Type I fluid to flow off (Figure 3.14). It quickly flows off the sensor leading to discontinuous coverage of the sensing electrodes.

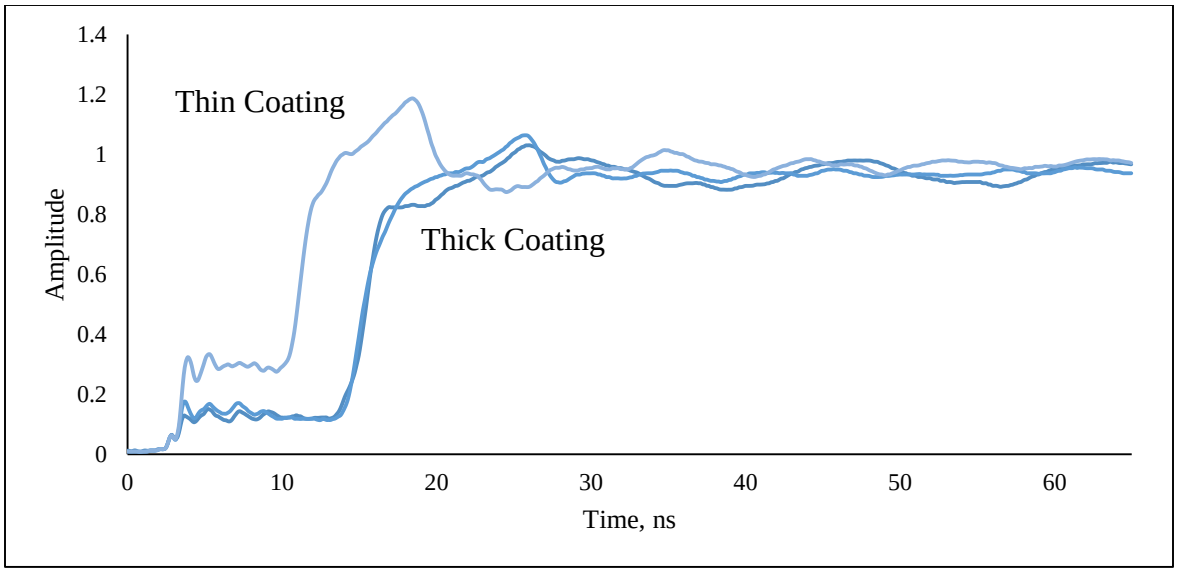

Figure 3.14 Waveforms collected from sensor B21 as Type I fluid was applied and the sensor was oriented vertically to allow the fluid to flow off the sensor.

Although, sample waveforms were found to vary as Type I fluids became discontinuous across the surface of a candidate sensor, waveforms collected with sensors oriented horizontally do not exhibit this trend. Therefore, care should be taken while sensors are mounted to aircraft surfaces in order to keep the orientation near horizontal.

3.4 Sensor Design with the Best Steady-State Performance

As stated in section 2.3, general sensor design aspects were drawn from previous experiments on bridge surface sensors,[12] but more elaborate sensors could be designed and tested due to the reduced ruggedness of an aircraft surface as compared to a bridge or road surface. From previous experiments with bridge surface sensors, it was known that small electrode gaps, low volume electrodes, and long path length sensors provide a lower FOM between ice and air.[12] The small electrode gap leads to greater penetration of the electric field into the medium in contact with the electrodes. Due to these trends, the sensors that performed the best were designed with thin electrode traces, small electrode gaps, and long path lengths. Only the sensor with the best performance, B11, will be presented here and the remainder will be presented in the appendices.

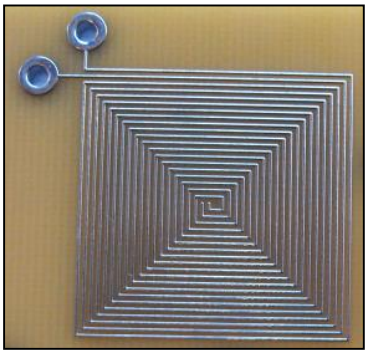

Figure 3.15 Sensor B11 measuring 1”x1”.

Table 3.4 Correlation array for sensor B11.

	Air	Water	Ice	Type I (50-50)	Type IV (50-50)
Air	3.000	0.072	1.210	0.030	0.142
Water	0.072	3.000	0.084	0.610	1.850
Ice	1.210	0.084	3.000	0.087	0.143
Type I (50-50)	0.030	0.610	0.087	3.000	1.875
Type IV (50-50)	0.142	1.850	0.143	1.875	3.000

Chapter 4. Non-Steady State Surface Conditions

4.1 Monitoring Phase Transitions Using Figure of Merit

Determining steady state conditions with a given sensor can be accomplished by selecting the highest correlation value of the sample waveform with a bank of standards using the figure of merit described in Chapter 3.1. This case only applies when the sample is uniform and covers the entire sensing area. When phase transitions are occurring, simple correlation fails to provide an adequate determination of the medium in contact with the sensor. In Figures 4.1 and 4.2 acquired waveforms and figure of merit values during a water freezing cycle are presented.

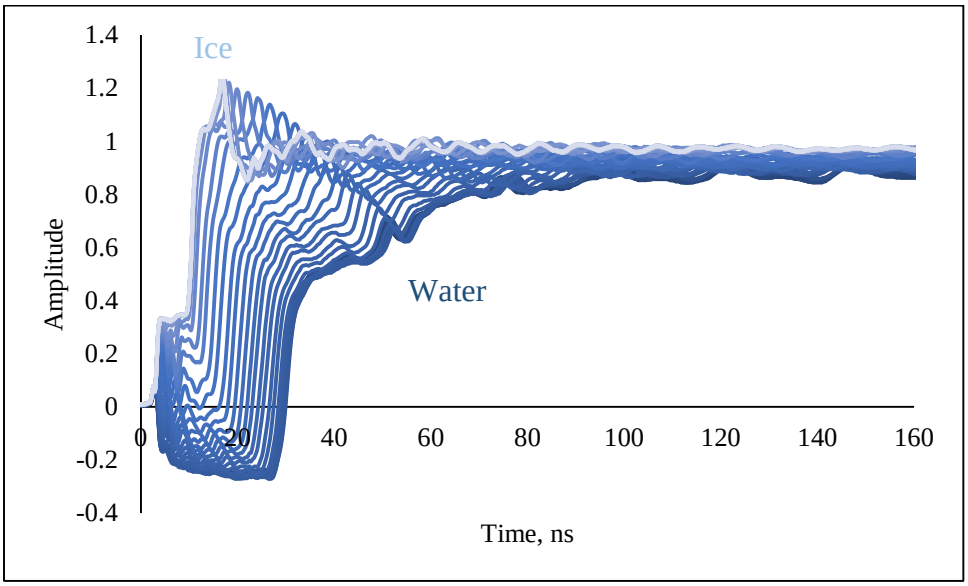

Figure 4.1 Subset of waveforms collected during a water freezing cycle.

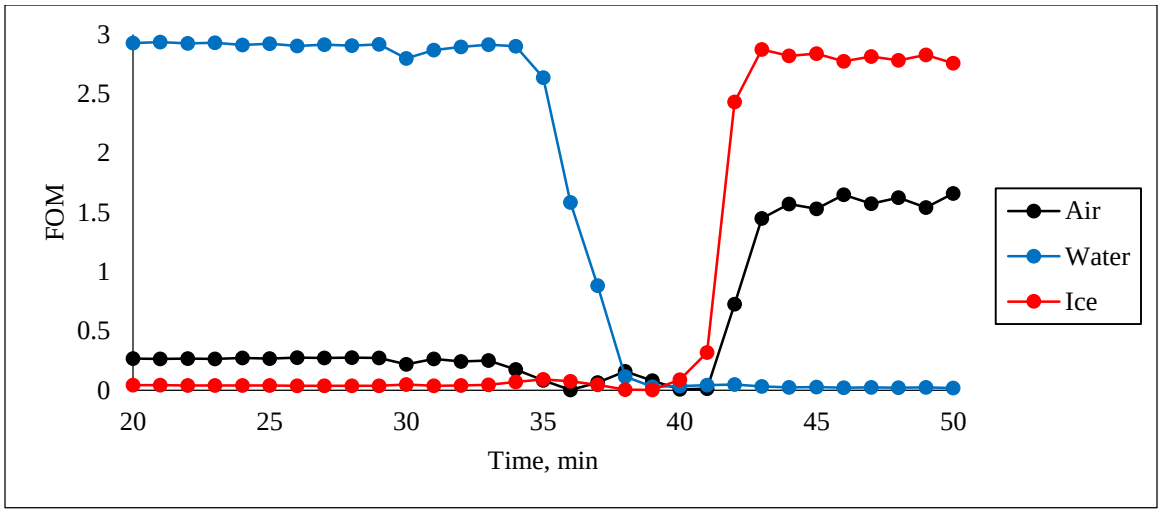

Figure 4.2 FOM trace of water freezing on sensor B21. Data was collected every minute, and the acquired data was correlated against previously acquired standards of air, water, and ice.

In order to model or predict phase transitions, characteristic transitions were captured with a variety of sensors. These transitions included: freezing of water, thawing of ice, freezing of ADAFs, thawing of ADAFs, addition of Type I fluid to ice, and addition of Type IV fluid to Type I fluid. With these transitions captured, many different methods of monitoring and predicting transitions were tested.

4.2 Software Protocol Development

Initially, the Fourier Transform was used to track the changes in characteristic frequencies that were unique to the dielectric relaxation of separate types of media. This method was shown to work with a number of the mentioned transitions, but not with all. A more robust method needed to be developed. The method that proved to provide consistent tracking of sensor conditions was a combination of correlation thresholds and point tracking.

To illustrate point tracking, a set of waveforms acquired during a water freezing cycle was analyzed to determine the maximum amplitude variation at each data point, shown below.

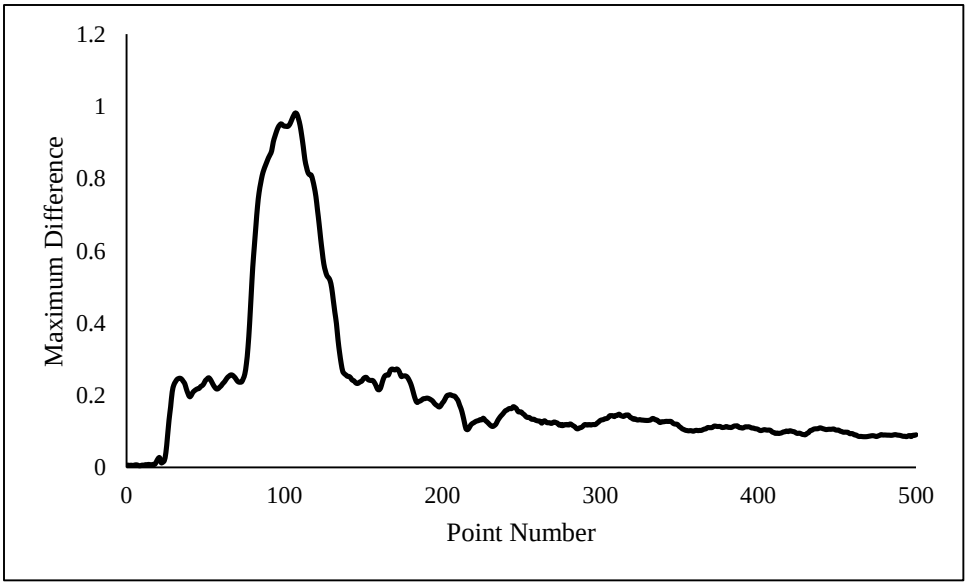

Figure 4.3 Maximum variation in the amplitude of each data point during a water freezing cycle with sensor B21.

With the point of maximum amplitude variation known, the point can be tracked during water, Type I, and Type IV freezing cycles.

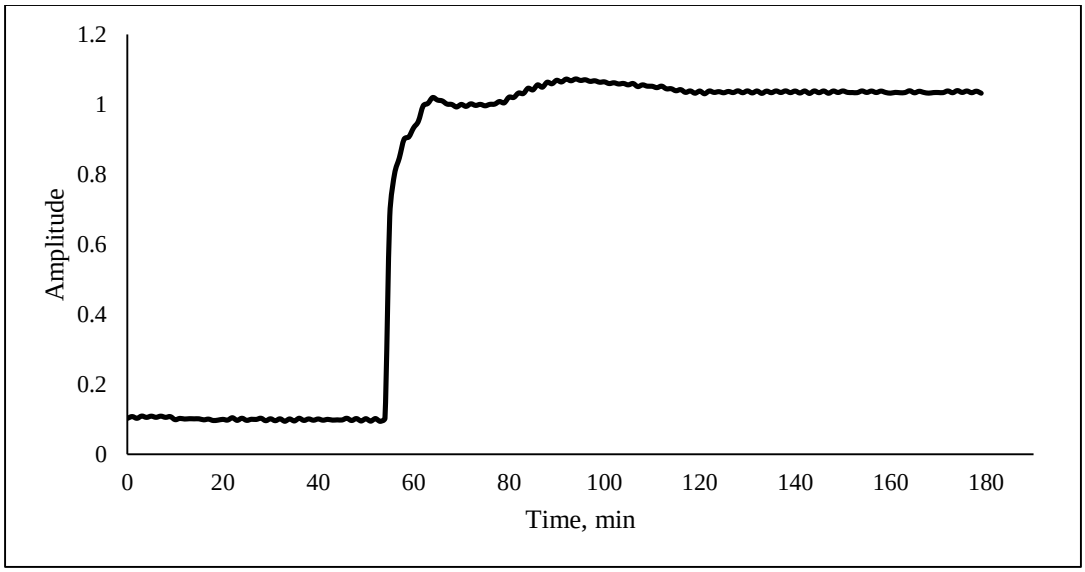

Figure 4.4 Tracking of point number 108 during a water freezing cycle with sensor B21. At zero minutes the sensor was coated with water and the temperature was lowered to -5ºC. As the water cooled and began to freeze at 53 minutes the amplitude of point 108 increased.

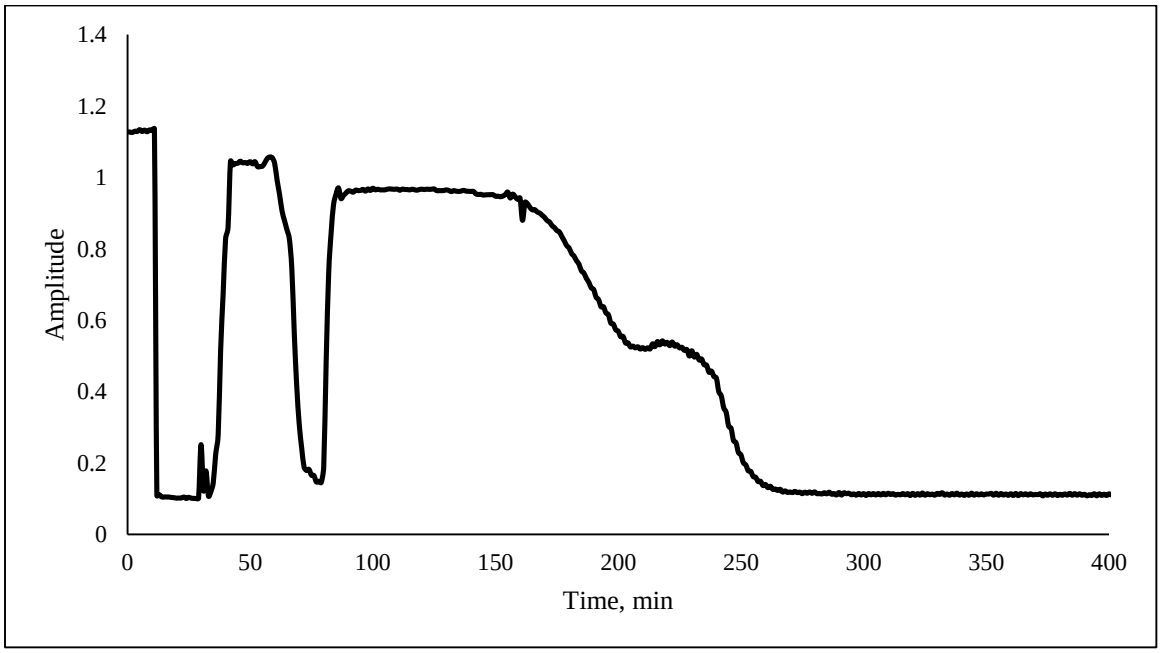

Figure 4.5 Tracking of point number 108 during a de-icing simulation with sensor B21. At zero minutes the sensor was dry and in contact with air. At 12 minutes water was poured over the sensor and the cooler was turned on. At 51 minutes 50/50 TypeI/water (by volume) was sprayed on top of the formed ice. At 74 minutes 50/50 TypeIV/water (by volume) was poured over the melted solution and dry ice was added. At 150 minutes the cooler was turned off and the dry ice removed.

Figure 4.5 illustrates that point tracking is able to reliably distinguish changes between the liquid and solid phase of water, Type I fluid, and Type IV fluid. Although, the point tracking method is able to provide the indication of phase changes, correlation must be introduced in order to determine the medium/media in contact with the sensor.

4.3 Software Protocol Optimization

In order to determine the medium/media in contact with a sensor during all de-icing/anti-icing situations, figure of merit and point tracking were combined.

Initially, standard files are collected with a candidate sensor (air, ice, water, 50/50 Type I/water, and 50/50 Type IV/water). Freezing cycles are then collected with water, 50/50 Type I/water, and 50/50 Type IV/water. The point of maximum variation during these freezing cycles is determined as in Figure 4.3. Once the minimum and maximum values of this point are determined, a threshold can be set between them. Any amplitude below this threshold is considered a safe situation, and any amplitude above this threshold is considered a hazardous situation. This threshold can then be optimized to alert personnel to the decrease in the dielectric constant before a hazardous condition is present. In addition, sample waveforms that are below the threshold are correlated with water, Type I fluid, and Type IV fluid and sample waveforms above the threshold are correlated with air, ice, frozen Type I fluid, and frozen Type IV fluid. If the figure of merit for an air standard during a hazardous situation is above 2.9 (calibrated for each sensor design), the condition is deemed safe. The flow diagram on the following page illustrates this technique. In order to test the reliability of the developed software, a number of sensors were subjected to icing/de-icing conditions. A figure of merit diagram is presented after the flow diagram that is characteristic of these cycles.

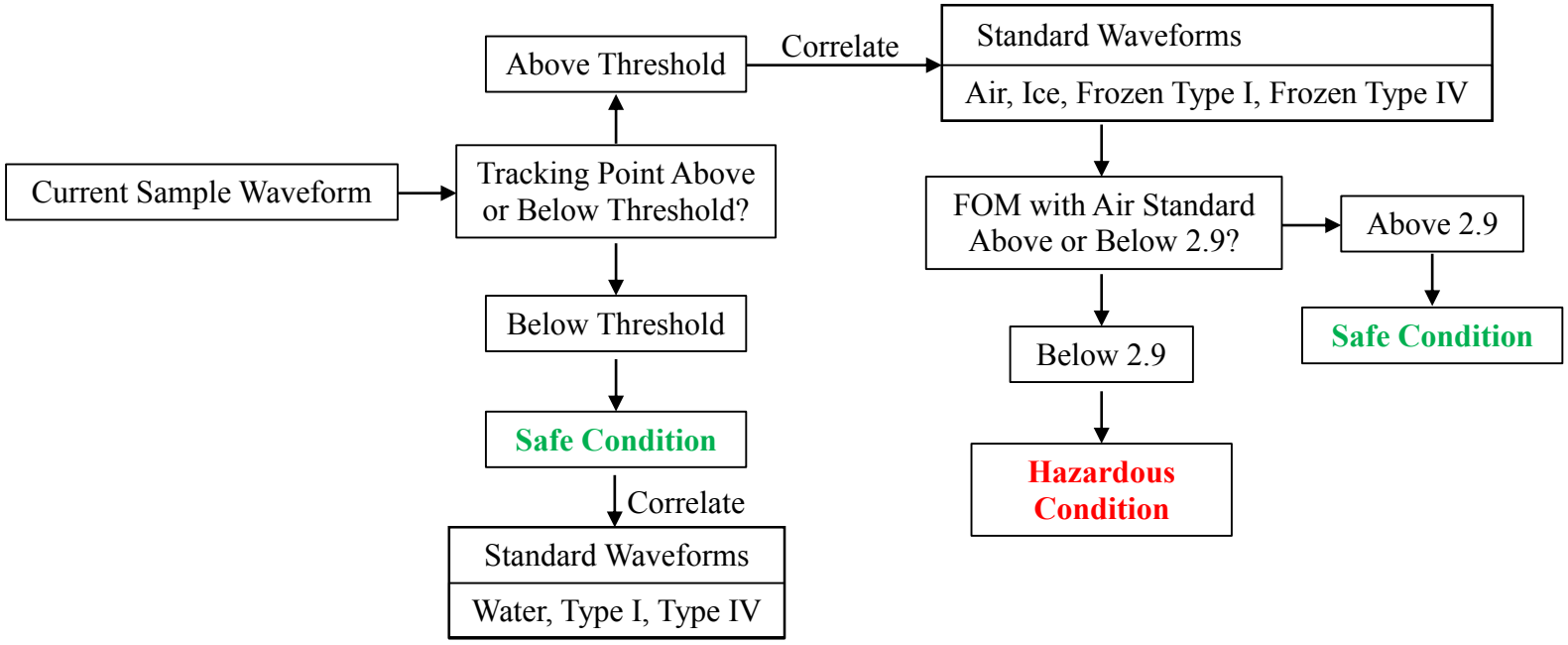

Figure 4.6 Flow diagram illustrating the LabVIEW software developed to determine safe and hazardous conditions.

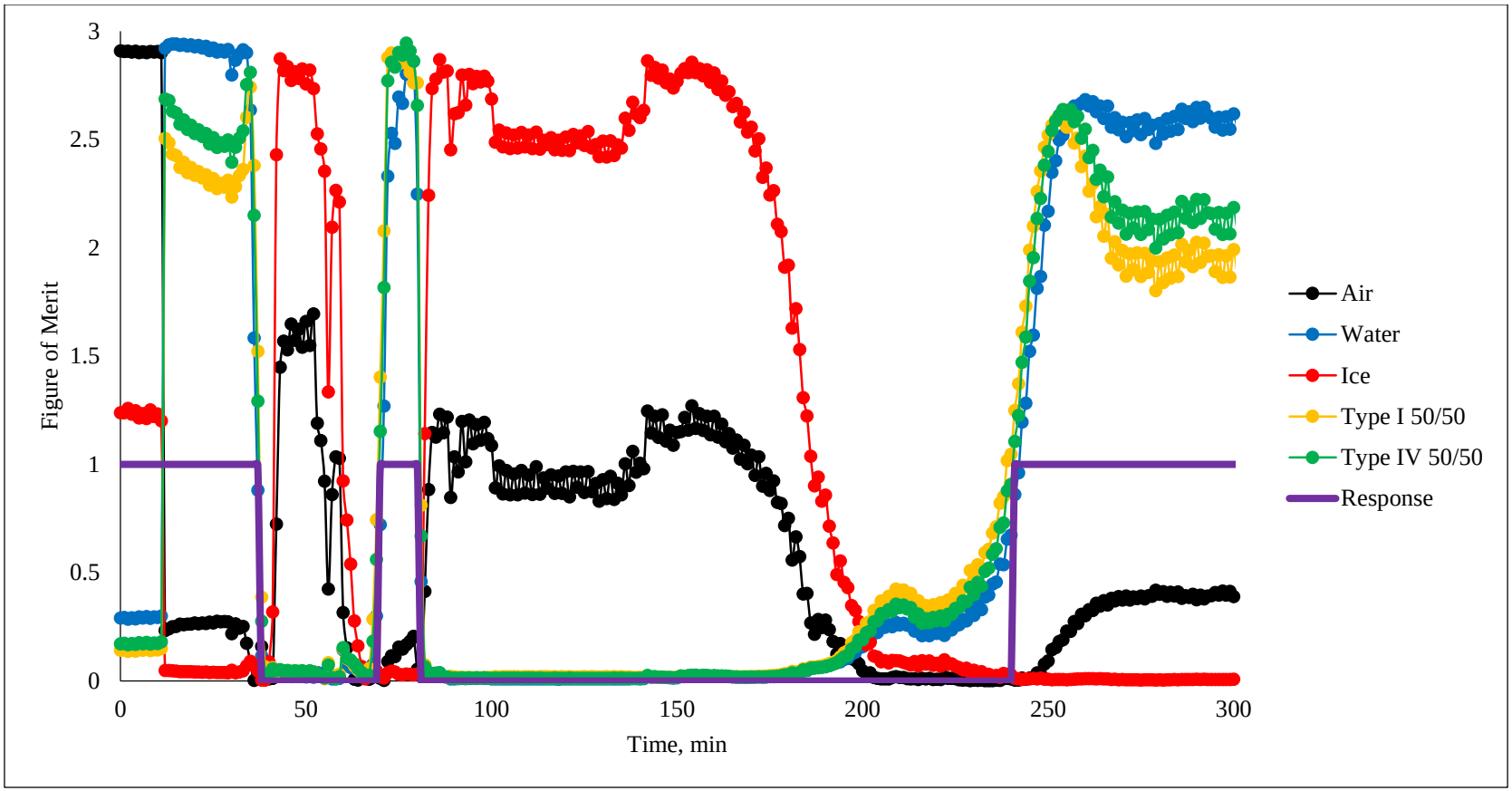

Figure 4.7 Tracking of FOM during a de-icing simulation with sensor B211. At zero minutes the sensor was dry and in contact with air. At 12 minutes water was poured over the sensor and the cooler was turned on. At 51 minutes 50/50 TypeI/water (by volume) was sprayed on top of the formed ice. At 74 minutes 50/50 TypeIV/water (by volume) was poured over the melted solution and dry ice was added. At 150 minutes the cooler was turned off and the dry ice removed. The binary response is returned from the LabVIEW program. A value of 1 indicates safe conditions and a value of 0 indicates hazardous conditions.

Figure 4.7 illustrates an icing/de-icing situation that would be typical of an aircraft surface. By following the binary response from the LabVIEW software, pilots and ground personnel would be able to reliably determine if conditions are suitable for flight or if de-icing needs to be carried out. In addition, ground personnel would be able to adjust the concentration of Type IV fluid used to lower the freezing point and provide adequate de-icing.

Chapter 5. Conclusions

5.1 Benefits of Study

The goal of this study was to demonstrate that TDR is an effective, reliable, and cost-effective technique for determining the surface conditions of aircraft. The system has been tested during multiple de-icing simulations (Figure 4.7) and has reliably determined safe and hazardous situations. The binary output of this system can provide pilots and ground personnel with conclusive information that can determine if an aircraft is safe for takeoff. It will also inform ground personnel when an aircraft is sufficiently de-iced which may assist in reducing the volume of ADAFs applied each season. The developed system is also cost-effective; aircraft of any size can be outfitted with the sensing system for under $12,000.

5.2 Future System Development and Field Testing

In order to test the sensing system in the field, sensors would be mounted at multiple locations of an aircraft that are the most likely to accumulate ice and frost (Figure 5.1).

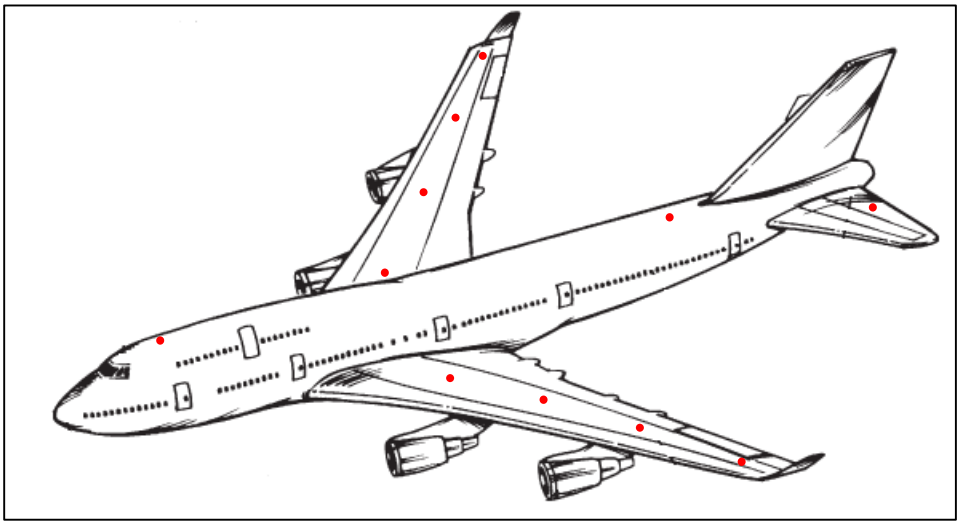

Figure 5.1 Diagram of sensors deployed on a commercial aircraft. Red dots indicated individual sensors.

The sensors would then be connected to a central processing location (TDR and datalogger) via 50Ω coaxial cables. The array of sensors will allow non-uniform conditions to be detected.

Once the sensor mounting locations are known, each sensor with its corresponding cable length can be calibrated using the technique outlined in Chapter 4.3. A bank of standards will be used for each sensor as in Figure 4.6. The output from each sensor can be combined to give an overall output indicating a safe or hazardous condition. On larger aircraft, each sensor output can be linked with an LED (red/green) readout to allow the pilot and ground personnel to know the exact location of ice accumulation.

References

1. Reehorst, A.; et al. Study of Icing Effects on Performance and Controllability of an Accident Aircraft. *Journal of Aircraft.* **2000,** 37 (2), 253–259.

2. Green, S.D. A Study of U.S. Inflight Icing Accidents and Incidents, 1978 to 2002, in: 44th AIAA Aerospace Sciences Meeting and Exhibit, Reno, Nevada, USA, January 9–12, 2006, AIAA2006-82.

3. Novak, L.; et al. Acute Toxicity of Storm Water Associated with De-icing/Anti-icing Activities at Canadian Airports. *Environmental Toxicology and Chemistry.* **2000,** 19 (7), 1846–1855.

4. Ge, J.; et al. A Novel Fiber-optic Ice Sensor Capable of Identifying Ice Type Accurately. *Sensors and Actuator A: Physical.* **2012,** 175, 35-42.

5. Heider, D.; Dominauskas, A. Composite Tech Brief, University of Delaware, Newark, DE (www.ccm.udel.edu), 2004.

6. Lin, C.P. Frequency Domain Versus Travel Time Analyses of TDR Waveforms for Soil Moisture Measurements. *Soil Sci. Soc. Am*. **2003,** 67, 720.

7. Robinson, D.A.; Jones, S.B.; Wraith, J.M.; Or, D.; Friedman, S.P. A Review of Advances in Dielectric and Electrical Conductivity Measurement in Soils Using Time Domain Reflectometry. *Vadose Zone J*. **2003,** 2, 444.

8. Seyfried, M.S.; Murdock, M.D. Calibration of Time Domain Reflectometry for Measurement of Liquid Water in Frozen Soils. *Soil Sci.* **1996,** 161, 87.

9. Yankielun, N.E.; Ryerson, C.C.; Jones, S.L. Wide-Area Ice Detection Using Time Domain Reflectometry. *US Army Corps of Engineers Tech*. **2002** Rpt. ERDC/CRREL TR-02-15.

10. Mashimo, S.; Miura, N.; Umehara, T. The Structure of Water Determined by Microwave Dielectric Study on Water Mixtures with Glucose, Polysaccharides, and L-ascorbic Acid. *J. Chem. Phys.* **1992,** 97, 6759.

11. Sakamoto, T.; Nakamura, H.; Uedaira, H.; Wada A. High-frequency Dielectric Relaxation of Water Bound to Hydrophilic Silica Gels. *J. Phys. Chem*. **1989**, 93, 357.

12. Evans, J. F. (2009) Detection of Water and Ice on Bridge Structures by AC Impedance and Dielectric Relaxation Spectroscopy Phase I,; (2013) Detection of Water and Ice on Bridge Structures by AC Impedance and Dielectric Relaxation Spectroscopy Phase II, Center for Transportation Studies, University of Minnesota,

200 Transportation and Safety Building, 511 Washington Ave. S.E., Minneapolis, MN 55455.

13. Bracewell, R. N. *The Fourier Transform and Its Applications*, 3rd ed.; McGraw-Hill: Boston, 2000.

14. Mallat, S. *A Wavelet Tour of Signal Processing*, 2nd ed.; Academic Press: San Diego, CA, 1999.

15. Qian S. *Introduction to Time-Frequency and Wavelet Transforms*, 1st ed.; Prentice Hall PTR: Upper Saddle River, New Jersey, 2001.

16. Daubechies, I. Ten Lectures on Wavelets, *IEE Trans. Signal Proc*. **1992**

17. Akansu, A.N.; Serdijn, W.A.; Selesnick, I. Emerging Applications of Wavelets: A Review. *Phys. Comm*. **2010**, 3, 1.

18. Strang, G. Wavelet Transforms vs Fourier Transforms, *Bull. Am. Math. Soc*. **1993**, 28, 288.

Appendix A. Sensors Designed for Preliminary Testing

Figure A.1 Sensor A1, 4”x0.1”.

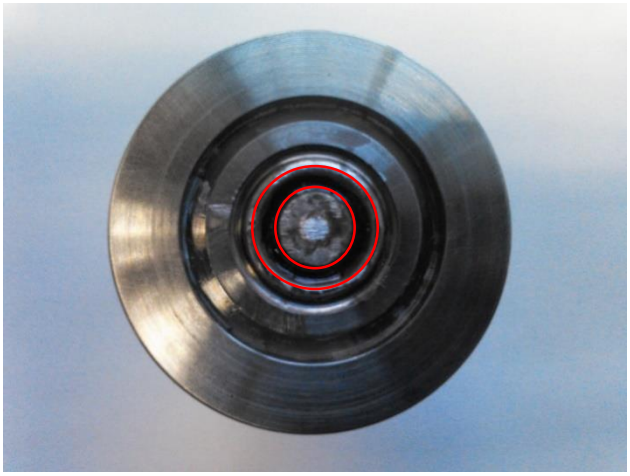

Figure A.2 Sensor A2, center electrode=0.1” OD.

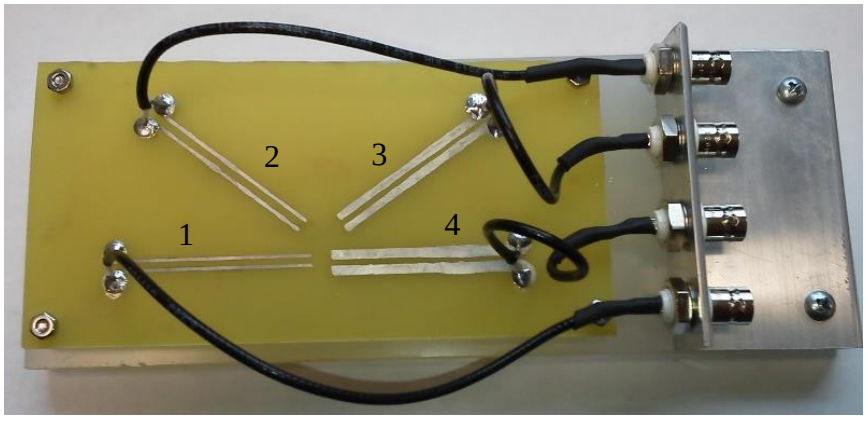

Figure A.4 Sensor A3. Each sensor is 2” long. Electrode widths: 1=0.025”, 2=0.030”, 3=0.075”, 4=0.100”.

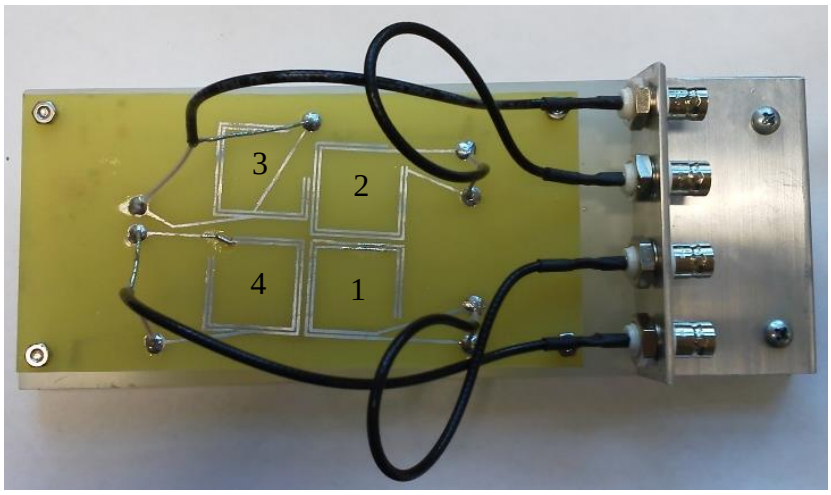

Figure A.5 Sensor A5. Each sensor is 1”x1”. Electrical connections: 1=same end, 2=opposite end, 3=1/3 after start, 4=end and 2/3 after start.

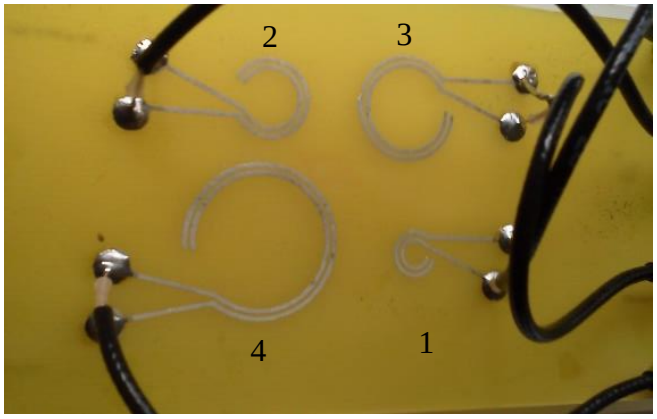

Figure A.6 Sensor A6. Electrode diameters: 1=0.3”, 2=0.5”, 3=0.7”, 4=1.0”.

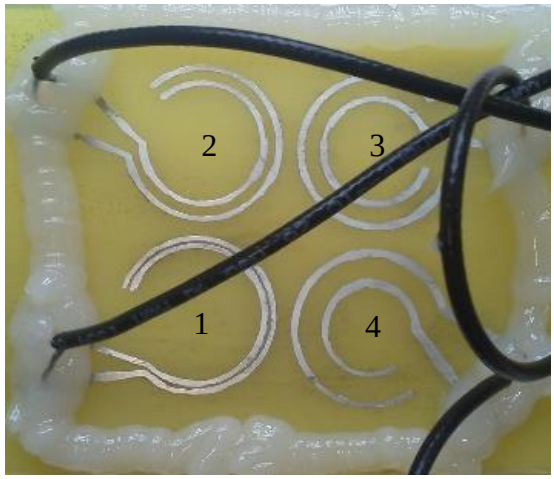

Figure A.6 Sensor A7. Each outer electrode diameter is 1”. Electrode gaps: 1=0.03”, 2=0.06”, 3=0.12”, 4=0.18”.

Appendix B. Printed Circuit Board Sensors and Correlation Arrays

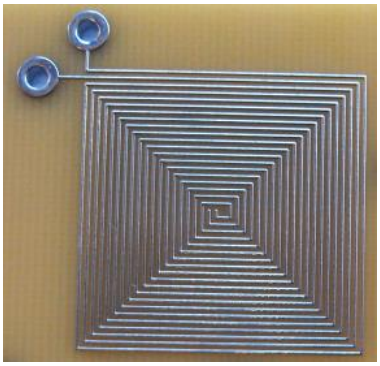

Figure B.1 Sensor B11, 1”x1”.

Table B.1 Correlation array for sensor B11.

	Air	Water	Ice	Type I (50-50)	Type IV (50-50)
Air	3.000	0.072	1.210	0.030	0.142
Water	0.072	3.000	0.084	0.610	1.850
Ice	1.210	0.084	3.000	0.087	0.143
Type I (50-50)	0.030	0.610	0.087	3.000	1.875
Type IV (50-50)	0.142	1.850	0.143	1.875	3.000

Figure B.2 Sensor B12, 1”x1”.

Table B.2 Correlation array for sensor B12.

	Air	Water	Ice	Type I (50-50)	Type IV (50-50)
Air	3.000	1.903	2.392	1.738	2.041
Water	1.903	3.000	1.439	2.720	2.748
Ice	2.392	1.439	3.000	1.263	1.436
Type I (50-50)	1.738	2.720	1.263	3.000	2.859
Type IV (50-50)	2.041	2.748	1.436	2.859	3.000

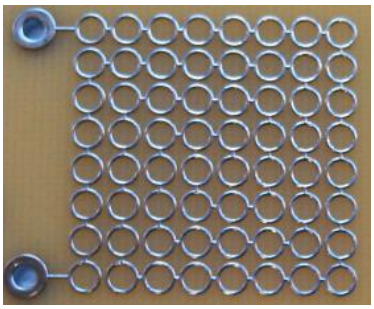

Figure B.3 Sensor B13, 1”x1”.

Table B.3 Correlation array for sensor B13.

	Air	Water	Ice	Type I (50-50)	Type IV (50-50)
Air	3.000	1.284	2.728	1.469	1.619
Water	1.284	3.000	1.376	2.334	2.648
Ice	2.728	1.376	3.000	1.536	1.714
Type I (50-50)	1.469	2.334	1.536	3.000	2.802
Type IV (50-50)	1.619	2.648	1.714	2.802	3.000

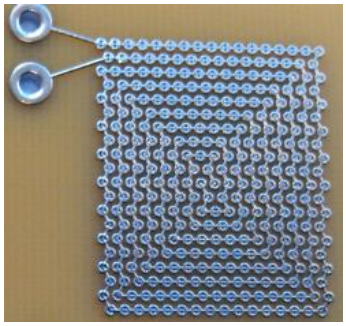

Figure B.4 Sensor B14, 1”x0.9”.

Table B.4 Correlation array for sensor B14.

	Air	Water	Ice	Type I (50-50)	Type IV (50-50)
Air	3.000	0.444	2.358	0.586	0.833
Water	0.444	3.000	0.788	1.876	2.530
Ice	2.358	0.788	3.000	1.060	1.252
Type I (50-50)	0.586	1.876	1.060	3.000	2.513
Type IV (50-50)	0.833	2.530	1.252	2.513	3.000

Figure B.5 Sensor B15, 0.5”x0.5”.

Table B.5 Correlation array for sensor B15.

	Air	Water	Ice	Type I (50-50)	Type IV (50-50)
Air	3.000	0.207	2.472	0.439	0.421
Water	0.207	3.000	0.147	1.441	2.073
Ice	2.472	0.147	3.000	0.482	0.377
Type I (50-50)	0.439	1.441	0.482	3.000	2.425
Type IV (50-50)	0.421	2.073	0.377	2.425	3.000

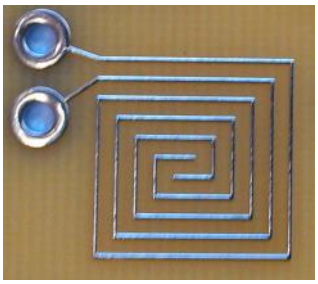

Figure B.6 Sensor B16, 0.5”x0.5”.

Table B.6 Correlation array for sensor B16.

	Air	Water	Ice	Type I (50-50)	Type IV (50-50)
Air	3.000	0.382	2.783	0.396	0.457
Water	0.382	3.000	0.375	1.487	1.995
Ice	2.783	0.375	3.000	0.405	0.454
Type I (50-50)	0.396	1.487	0.405	3.000	2.635
Type IV (50-50)	0.457	1.995	0.454	2.635	3.000

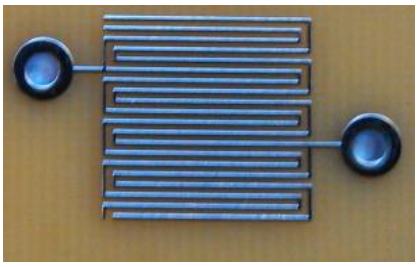

Figure B.7 Sensor B17, 0.5”x0.5”.

Table B.7 Correlation array for sensor B17.

	Air	Water	Ice	Type I (50-50)	Type IV (50-50)
Air	3.000	1.910	2.335	1.850	2.028
Water	1.910	3.000	2.037	2.676	2.753
Ice	2.335	2.037	3.000	1.650	1.880
Type I (50-50)	1.850	2.676	1.650	3.000	2.948
Type IV (50-50)	2.028	2.753	1.880	2.948	3.000

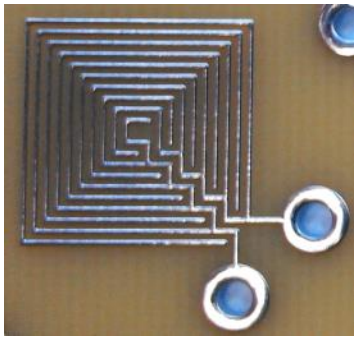

Figure B.8 Sensor B18, 0.5”x0.5”.

Table B.8 Correlation array for sensor B18.

	Air	Water	Ice	Type I (50-50)	Type IV (50-50)
Air	3.000	1.674	2.723	1.516	1.752
Water	1.674	3.000	1.257	2.301	2.555
Ice	2.723	1.257	3.000	1.046	1.242
Type I (50-50)	1.516	2.301	1.046	3.000	2.852
Type IV (50-50)	1.752	2.555	1.242	2.852	3.000

Figure B.9 Sensor B19, 0.5”x0.5”.

Table B.9 Correlation array for sensor B19.

	Air	Water	Ice	Type I (50-50)	Type IV (50-50)
Air	3.000	0.495	2.975	0.089	0.289
Water	0.495	3.000	0.470	2.597	2.877
Ice	2.975	0.470	3.000	0.075	0.268
Type I (50-50)	0.089	2.597	0.075	3.000	2.896
Type IV (50-50)	0.289	2.877	0.268	2.896	3.000

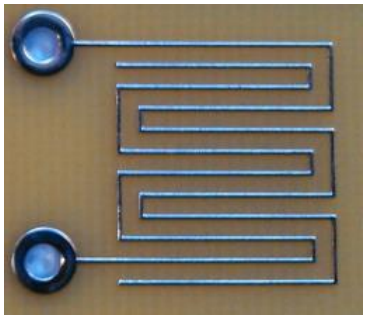

Figure B.10 Sensor B110, 0.5”x0.5”.

Table B.10 Correlation array for sensor B110.

	Air	Water	Ice	Type I (50-50)	Type IV (50-50)
Air	3.000	0.737	2.772	0.544	0.708
Water	0.737	3.000	0.940	2.612	2.838
Ice	2.772	0.940	3.000	0.693	0.905
Type I (50-50)	0.544	2.612	0.693	3.000	2.916
Type IV (50-50)	0.708	2.838	0.905	2.916	3.000

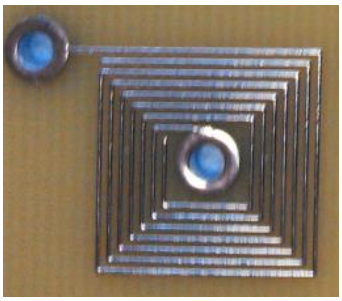

Figure B.11 Sensor B111, 0.5”x0.5”.

Table B.11 Correlation array for sensor B111.

	Air	Water	Ice	Type I (50-50)	Type IV (50-50)
Air	3.000	0.069	1.322	0.027	0.034
Water	0.069	3.000	0.257	2.268	2.552
Ice	1.322	0.257	3.000	0.116	0.152
Type I (50-50)	0.027	2.268	0.116	3.000	2.862
Type IV (50-50)	0.034	2.552	0.152	2.862	3.000

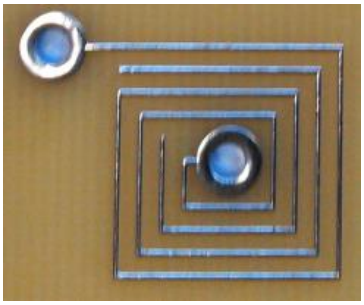

Figure B.12 Sensor B112, 0.5”x0.5”.

Table B.12 Correlation array for sensor B112.

	Air	Water	Ice	Type I (50-50)	Type IV (50-50)
Air	3.000	0.010	2.651	0.067	0.035
Water	0.010	3.000	0.012	2.120	2.512
Ice	2.651	0.012	3.000	0.111	0.067
Type I (50-50)	0.067	2.120	0.111	3.000	2.815
Type IV (50-50)	0.035	2.512	0.067	2.815	3.000

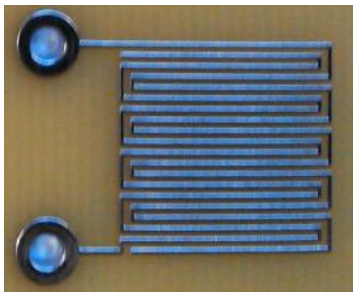

Figure B.13 Sensor B113, 0.5”x0.5”.

Table B.13 Correlation array for sensor B113.

	Air	Water	Ice	Type I (50-50)	Type IV (50-50)
Air	3.000	1.120	2.225	1.198	1.211
Water	1.120	3.000	1.753	2.676	2.767
Ice	2.225	1.753	3.000	1.548	1.651
Type I (50-50)	1.198	2.676	1.548	3.000	2.939
Type IV (50-50)	1.211	2.767	1.651	2.939	3.000

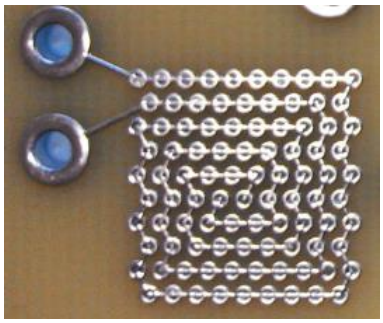

Figure B.14 Sensor B114, 0.5”x0.5”.

Table B.14 Correlation array for sensor B114.

	Air	Water	Ice	Type I (50-50)	Type IV (50-50)
Air	3.000	0.991	2.745	1.090	1.131
Water	0.991	3.000	0.952	2.050	2.392
Ice	2.745	0.952	3.000	0.987	1.041
Type I (50-50)	1.090	2.050	0.987	3.000	2.760
Type IV (50-50)	1.131	2.392	1.041	2.760	3.000

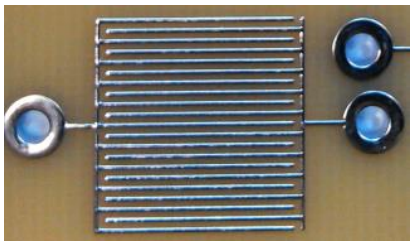

Figure B.15 Sensor B115, 0.5”x0.5”.

Table B.15 Correlation array for sensor B115.

	Air	Water	Ice	Type I (50-50)	Type IV (50-50)
Air	3.000	1.683	2.664	1.491	1.635
Water	1.683	3.000	0.891	2.958	2.976
Ice	2.664	0.891	3.000	0.723	0.823
Type I (50-50)	1.491	2.958	0.723	3.000	2.975
Type IV (50-50)	1.635	2.976	0.823	2.975	3.000

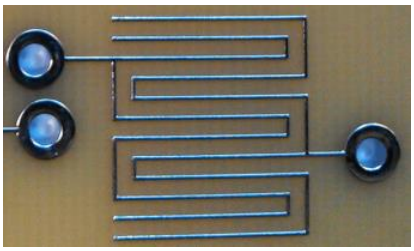

Figure B.16 Sensor B116, 0.5”x0.5”.

Table B.16 Correlation array for sensor B116.

	Air	Water	Ice	Type I (50-50)	Type IV (50-50)
Air	3.000	1.109	2.918	0.747	1.066
Water	1.109	3.000	1.092	2.622	2.828
Ice	2.918	1.092	3.000	0.720	1.068
Type I (50-50)	0.747	2.622	0.720	3.000	2.871
Type IV (50-50)	1.066	2.828	1.068	2.871	3.000

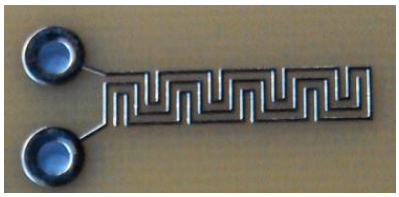

Figure B.17 Sensor B117, 0.5”x0.2”.

Table B.17 Correlation array for sensor B117.

	Air	Water	Ice	Type I (50-50)	Type IV (50-50)
Air	3.000	0.796	2.885	0.709	0.856
Water	0.796	3.000	0.867	2.350	2.768
Ice	2.885	0.867	3.000	0.689	0.868
Type I (50-50)	0.709	2.350	0.689	3.000	2.834
Type IV (50-50)	0.856	2.768	0.868	2.834	3.000